

# Chapter 5

## Results

---

### 5.1 Introduction

The results of the analysis, as described thus far, are shown in this chapter. The optimum geometry and optimum operating conditions for a system with maximum net power output are shown and discussed. Before these results are shown, a validation is done. The validation is done to better understand the effect of the compressor, turbine and recuperator efficiencies on the thermal efficiency of the system. The validation confirms that an optimum operating condition exists for the recuperative open and direct solar thermal Brayton cycle. The first validation shows that the thermal efficiency of the system can be derived in terms of the compressor pressure ratio, compressor efficiency, turbine efficiency, recuperator efficiency and the inlet temperatures of the compressor and turbine as constants. The derivations are compared with equations from the literature.

As a second validation, the net power output is calculated using equation 3.61. In this validation, the temperatures and pressures required to calculate the net power output are calculated using assumptions of pressure and temperature drops across the components. Again, it is evident that an optimum operating condition exists. The pressure and temperature losses should, however, be described in terms of the geometry variables of the system, but in the second validation they are assumed to be constant. The net power output (equation 3.61) as a function of compressor pressure ratio is compared with the net power output as calculated from the first law of thermodynamics.

For the full analysis, the numerical and geometrical model and temperatures and pressures, as discussed in the previous sections, are used. The temperatures and pressures used in the objective function are calculated as shown in Section 3.6. The geometries are thermodynamically optimised and the optimum operating conditions are shown.

## 5.2 Validation

### 5.2.1 First validation

One would like to have the thermal efficiency of the system in terms of the efficiency of the recuperator and the isentropic efficiencies of the turbine and compressor. This thermal efficiency curve should give a hint of whether or not a maximum exists in terms of the pressure ratio of the cycle. In this first part of the validation, it is assumed that  $r = P_2 / P_1 = P_3 / P_4$  as is shown in Figure 5.1. The thermal efficiency is also written as a function of  $T_1$  and  $T_3$ . This section starts off with a derivation of the thermal efficiency of the cycle, without any recuperation and excluding the isentropic efficiencies of the compressor and turbine. The section ends with an equation for the thermal efficiency, which includes the efficiency of the recuperator and the isentropic efficiencies of the compressor and turbine.

#### 5.2.1.1 Thermal efficiency - no recuperator ( $\eta_c$ and $\eta_t = 1$ )

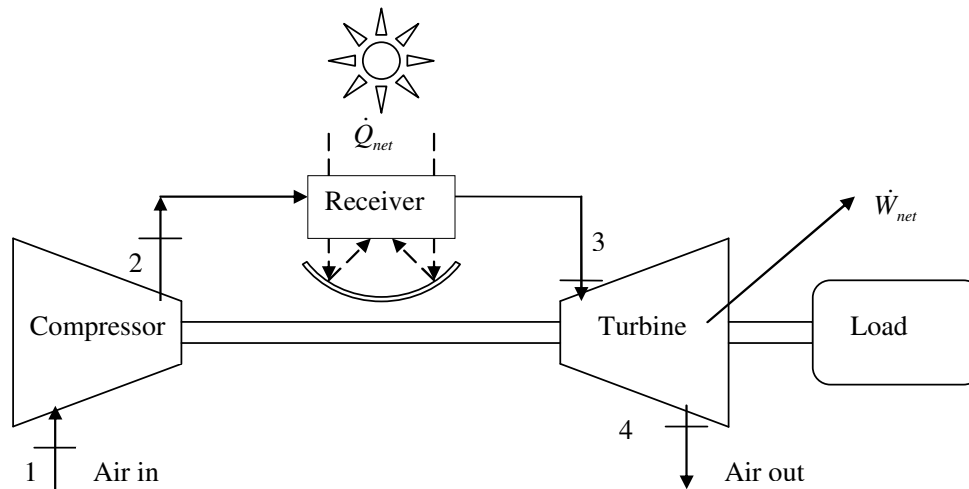


Figure 5.1 The open and direct solar thermal Brayton cycle with no recuperator (Stine and Harrigan, 1985).

Figure 5.1 shows the open solar thermal Brayton cycle without recuperation. The thermal efficiency is defined as:

$$\eta_{th} = \frac{w_{net}}{q_{net}} = \frac{w_t / w_c - 1}{q_{net} / w_c} \quad (5.1)$$

where  $q_{net}$  is the net accepted specific heat in the receiver. It can be shown that, for no recuperation and 100% compressor and turbine efficiencies, the thermal efficiency is:

$$\eta_{th} = \frac{w_{net}}{q_{net}} = \frac{K-1}{K} = 1 - 1/K \quad (5.2)$$

since  $\frac{w_t}{|w_c|} = \left(\frac{T_3}{T_1}\right) / K$  (Weston, 2000),  $K = \left(\frac{P_2}{P_1}\right)^{k-1/k}$  and  $w_{net} = w_t - w_c$ . Also note that equation 5.2 is derived by writing  $w_c$  and  $q_{net}$  in terms of the temperatures. Equation 5.2 is confirmed with Weston (2000) and Stine and Harrigan (1985).

### 5.2.1.2 Thermal efficiency - with recuperator ( $\eta_{reg} < 1$ and $\eta_c$ and $\eta_t = 1$ )

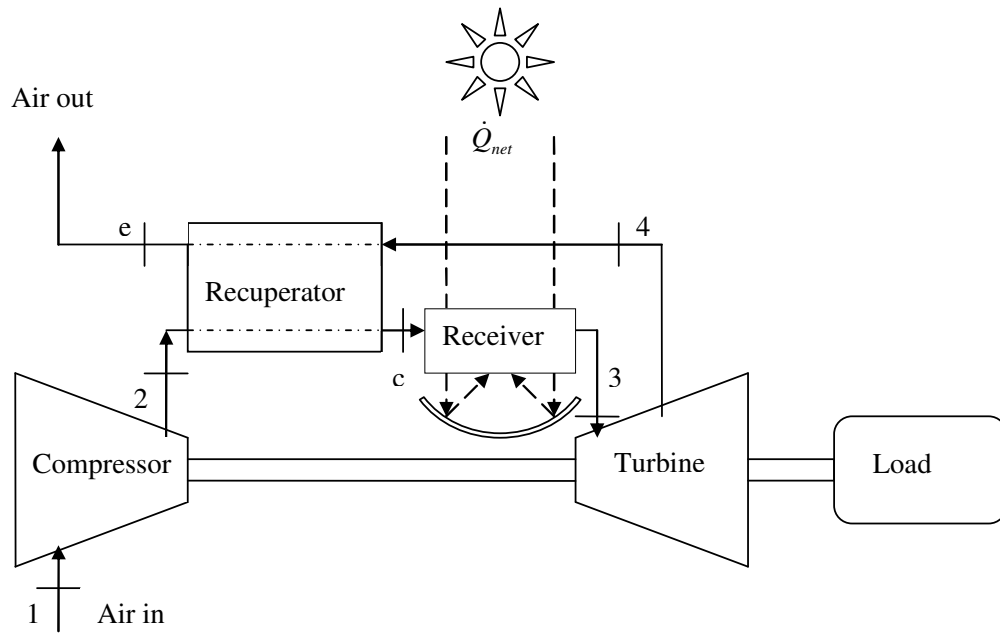


Figure 5.2 The open and direct solar thermal Brayton cycle with recuperator (Weston, 2000).

The inclusion of the recuperator is shown in Figure 5.2. According to Weston (2000), the efficiency of the recuperator can be defined with equation 5.3.

$$\eta_{reg} = \frac{(T_c - T_2)}{(T_4 - T_2)} \quad (5.3)$$

The addition of the recuperator efficiency and 100% compressor and turbine efficiencies results in the following thermal efficiency equation:

$$\eta_{th} = \frac{(K-1) \left( 1 - \left( \frac{T_1}{T_3} \right) K \right)}{K - \eta_{reg} + (\eta_{reg} - 1) \left( \frac{T_1}{T_3} \right) K^2} \quad (5.4)$$

When  $\eta_{reg} = 0$ , equation 5.4 becomes equation 5.2. When  $\eta_{reg} = 1$ , equation 5.4 becomes

$$\eta_{th} = 1 - \left( \frac{T_1}{T_3} \right) K \quad (5.5)$$

Equation 5.5 is also given by Stine and Harrigan (1985) and is shown in Figure 2.6. In this figure, the thermal efficiency curves of  $\eta_{reg} = 0$  and  $\eta_{reg} = 1$  are compared. Equation 5.4 is plotted in Figure 5.3 for  $T_3 = 1\,200\text{ K}$ ,  $T_1 = 300\text{ K}$  and  $\eta_{reg} = 0.77$ . Also plotted are the curves where  $\eta_{reg} = 0$  (equation 5.2) and  $\eta_{reg} = 1$  (equation 5.5). Figure 2.5 from the literature study gives a similarly shaped curve for  $0 < \eta_{reg} < 1$ .

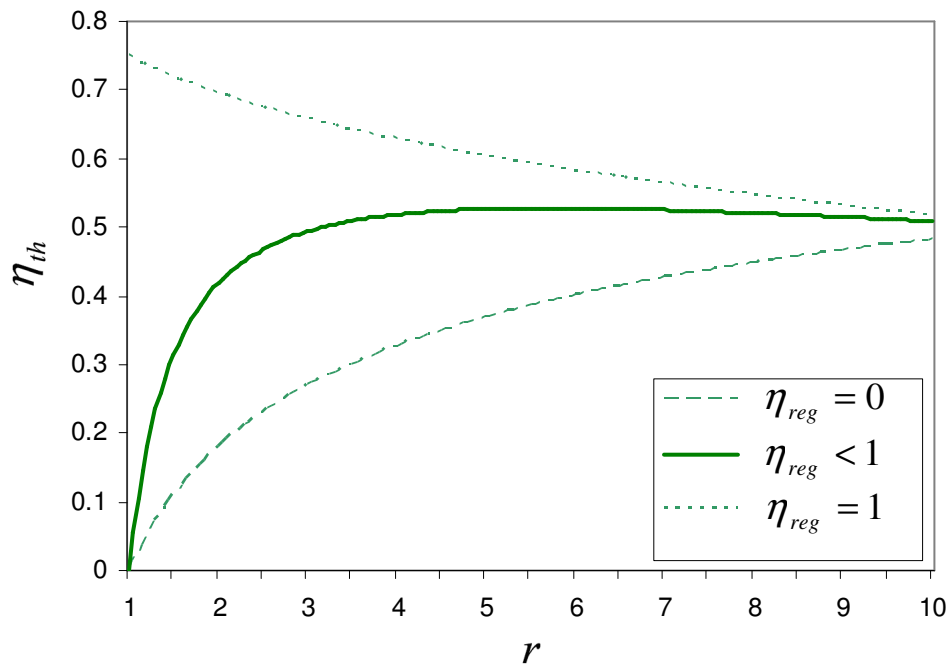


Figure 5.3 Comparison of the thermal efficiency of the Brayton cycle for different cases of recuperation.

Figure 5.3 shows that an optimum thermal efficiency exists when a recuperator is used. Also, this optimum is at a much lower pressure ratio than if the recuperator is not used. The advantages of recuperation are clearly shown. The thermal efficiency curve is bounded by the two curves representing no recuperator and 100% recuperator efficiency respectively.

### 5.2.1.3 Thermal efficiency - with recuperator and isentropic efficiencies ( $\eta_{reg}, \eta_c, \eta_t < 1$ )

The next step would be to include the isentropic efficiency of the turbine and the compressor to see what effect it would have on the thermal efficiency curves. It can be shown that

$$T_2 = T_1 \left[ 1 + (K - 1) / \eta_c \right] \quad (5.6)$$

and

$$T_4 = T_3 \left[ 1 - \eta_t \left( 1 - \frac{1}{K} \right) \right] \quad (5.7)$$

For this case:

$$\frac{w_t}{|w_c|} = \left( \frac{T_3}{T_1} \right) \frac{\eta_t \eta_c}{K} \quad (5.8)$$

Equation 5.9 shows the thermal efficiency in terms of the recuperator, compressor and turbine efficiencies.

$$\eta_{th} = \left[ \frac{\eta_c \eta_t \left( \frac{T_3}{T_1} \right) - K}{K} \right] \left[ \frac{K - 1}{\eta_c \left( \frac{T_3}{T_1} \right) - \eta_c - (K - 1) - \eta_{reg} \eta_c \left( \frac{T_1}{T_3} \right) \left[ 1 - \eta_t \left( 1 - \frac{1}{K} \right) \right] + \eta_{reg} \eta_c + \eta_{reg} (K - 1)} \right] \quad (5.9)$$

When  $\eta_{reg} = 0$ , equation 5.9 becomes

$$\eta_{th} = \frac{T_3 \eta_c \eta_t - T_1 K}{T_3 K \left( \frac{\eta_c}{K-1} \right) - T_1 K \left( \frac{\eta_c}{K-1} \right) - T_1 K} \quad (5.10)$$

When  $\eta_{reg} = 1$ , equation 5.9 becomes

$$\eta_{th} = \left[ \frac{\left( \frac{T_3}{T_1} \right) \eta_c \eta_t - K}{K} \right] \left[ \frac{K-1}{\eta_c \eta_t \left( \frac{T_3}{T_1} \right) \left( 1 - \frac{1}{K} \right)} \right] \quad (5.11)$$

Figure 5.4 shows equations 5.9 - 5.11 together with the results of Figure 5.3 (where the isentropic efficiencies were assumed to be 100%).

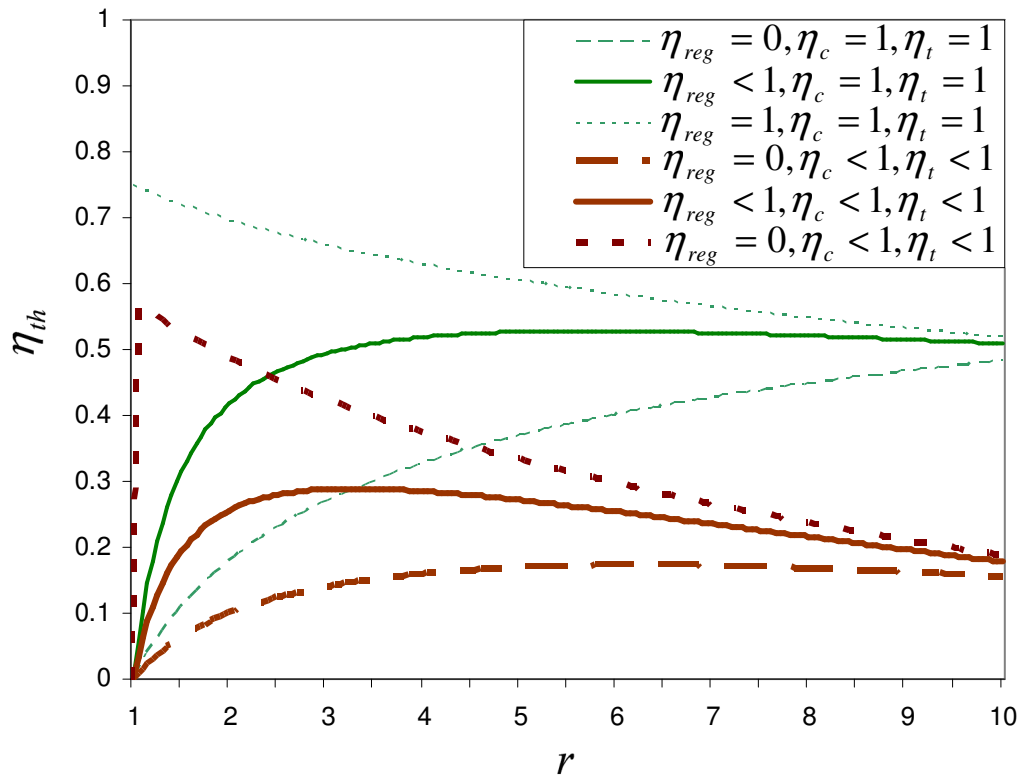


Figure 5.4 The thermal efficiency as a function of pressure ratio for different recuperation situations.

The same shape is generated in Figure 5.4 than in Figure 5.3, except that the curve has shifted lower, due to the isentropic efficiencies of the turbine and compressor being smaller than one. In

this figure,  $T_3 = 1\ 200\ \text{K}$ ,  $T_1 = 300\ \text{K}$ ,  $\eta_{reg} = 0.77$ , 0 or 1 and  $\eta_c$  and  $\eta_t = 1$  or 0.77. It is also shown in Figure 5.4 that a shallow optimum exists. This optimum depends on the temperatures,  $T_1$  and  $T_3$ , and the efficiencies of the recuperator, compressor and turbine, as shown in equation 5.9. The thermal efficiency curve is again bounded by two curves from above and below.

### 5.2.2 Second validation

The net power output is the only reason for interest in the Brayton cycle, or any solar thermal power system for that matter. In equation 3.61, the net power output was defined in terms of the entropy generation rate at each component and duct in the system. By having a similar approach than for the thermal efficiencies in the previous section, equation 3.61 can be plotted as a function of the pressure ratio ( $r = P_2 / P_1$ ) only. For this analysis, all the pressure drops and temperature losses in the system are assumed to be constant.  $P_3 / P_4$  will not be assumed equal to  $r$  and  $T_3$  will be a function of  $r$  and not a constant. The system mass flow rate is assumed to be a linear function of  $r$ . Note that the geometry variables are not yet included. There are also no material constraints for any of the temperatures. All the temperatures and pressures for Figure 3.5 were calculated in a spreadsheet at each pressure ratio,  $r$ , by performing an iteration (similar to Section 3.6). The constants used are given in Table 5.1.

The net power output can be plotted in terms of the pressure ratio. Since equation 3.61 was used, the net power output was calculated using the second law of thermodynamics. When plotting the net power output in terms of the first law of thermodynamics with the following equation:

$$\dot{W}_{net, FirstLaw} = \dot{m}c_p (T_7 - T_8 + T_1 - T_2),$$

the first and second law curves can be compared.

Equation 3.61 is plotted in Figure 5.5, together with the net power output calculated from the first law of thermodynamics.

Note that these functions were calculated using the temperatures and pressures found with the iteration process and using the constants in Table 5.1. The curves in Figure 5.5 are of the same shape as the thermal efficiencies in Section 5.2.1. For both curves (from the first and second laws of thermodynamics) in Figure 5.5, an optimum exists at a pressure ratio of approximately 1.6. For the second law, the contribution from the ducts to the total entropy generation was assumed negligible and might be the reason for the small difference between these curves. The close comparison of the curves in Figure 5.5 shows that the net power output from equation 3.61 is correctly described in terms of the total entropy generation rate in the system.

**Table 5.1 Assumptions for second validation.**

<b>Definition</b>	<b>Value</b>	<b>Units</b>
$\eta_{reg}$	0.8	-
$\eta_c$	0.73	-
$\eta_t$	0.73	-
$R$	287	J/kgK
$c_p$	1004	J/kgK
$T_1$	300	K
$\Delta T_{23}$	2	K
$\Delta T_{45}$	2	K
$\Delta T_{67}$	2	K
$\Delta T_{89}$	2	K
$P_1$	80	kPa
$\Delta P_{23}$	0.1	%
$\Delta P_{34}$	1	%
$\Delta P_{45}$	0.4	%
$\Delta P_{56}$	0.8	%
$\Delta P_{67}$	0.4	%
$\Delta P_{89}$	0.1	%
$\Delta P_{910}$	1	%
$\dot{Q}_{loss,23}$	2	W
$\dot{Q}_{loss,45}$	2	W
$\dot{Q}_{loss,67}$	2	W
$\dot{Q}_{loss,89}$	2	W
$\dot{Q}_{loss,reg}$	2	W
$\dot{Q}_{rec}^*$	64 000	W
$\dot{Q}_{loss,rec}$	6 400	W

At higher pressure ratios, the net power output becomes negative, which means that the power output of the turbine is smaller than the power required from the compressor. Such a system would not be possible. However, these data points show the rate of decrease in net power output as the pressure ratio increases, at higher pressure ratios.



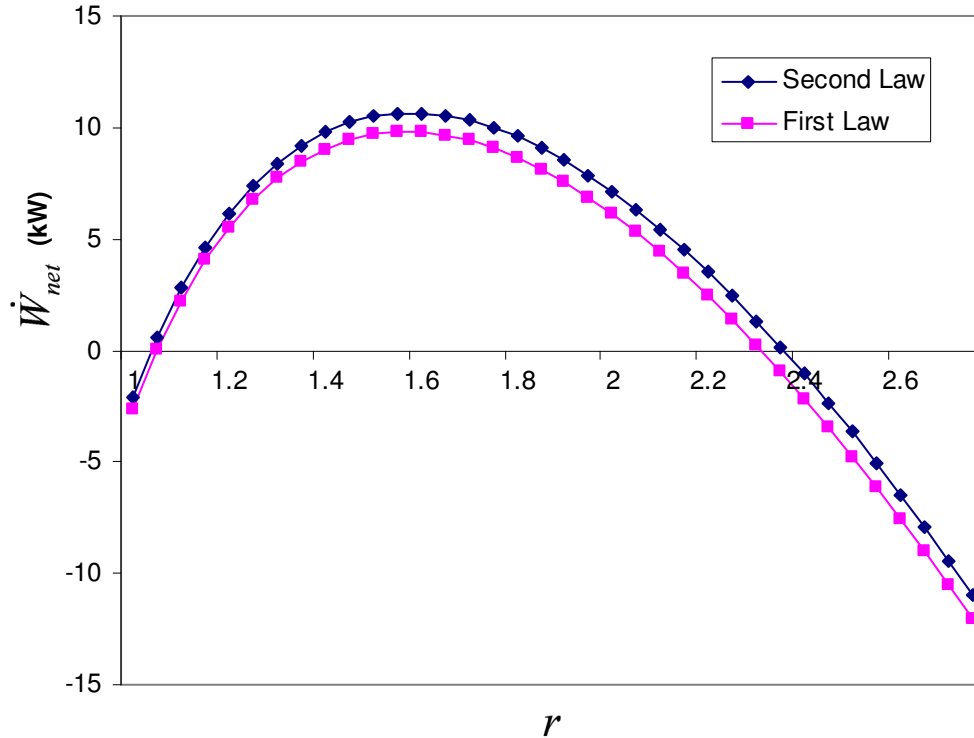


**Figure 5.5 Net power output calculated with the first and second laws of thermodynamics as a function of the pressure ratio.**

The thermal efficiencies are plotted in Figure 5.6, for different assumptions for the compressor, turbine and recuperator efficiencies (similar to Section 5.2.1.3). The thermal efficiency curve is bounded by two curves. When comparing this figure with Figure 5.4, it seems that the thermal efficiency drops quicker in Figure 5.6. It is as if the curves are 'pulled' downwards. This can be because  $T_3$  is no longer a constant (as in Section 5.2.1), but is now also a function of the compressor pressure ratio. This is a much more realistic curve than the curve shown in Figure 5.3. Also note that the curve, where no recuperator is used and the isentropic efficiencies are included, is not shown. This curve did not appear in the positive region (making a working system with no recuperator and real compressor and turbine efficiencies impossible). The method of entropy generation can be used to get the optimum receiver and recuperator geometries which could 'lift' the thermal efficiency curve to higher values.

Figure 5.7 shows the contribution of the turbine, compressor, recuperator and solar receiver to the total entropy generation rate, based on the assumptions in Table 5.1. The entropy generation rate in the ducts was very small compared with the other components and was neglected. The entropy generation rate in a duct would be very small if the duct is well-insulated and if it has a large hydraulic diameter.

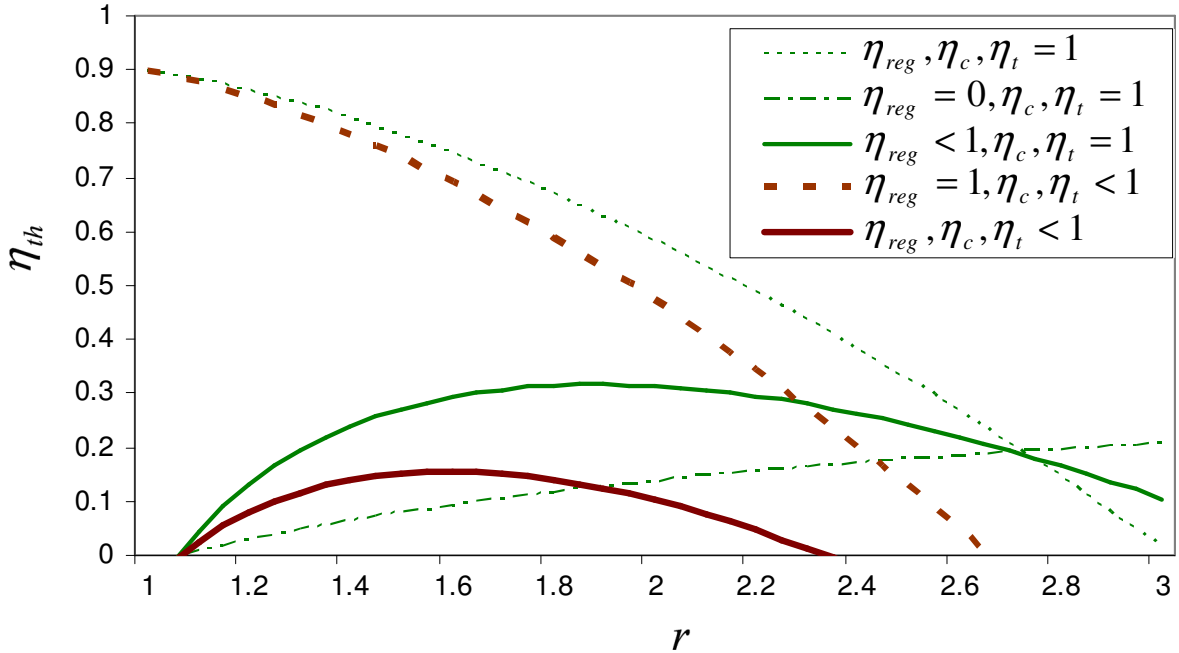


Figure 5.6 Thermal efficiency as a function of the pressure ratio.

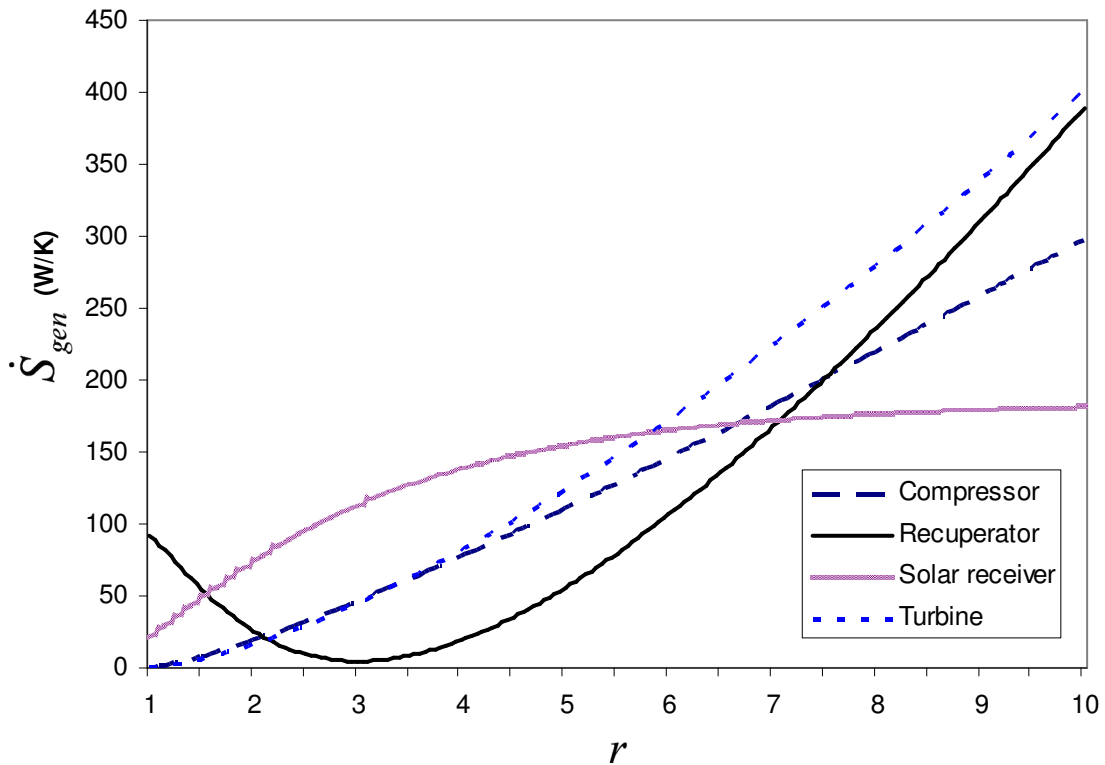


Figure 5.7 Contribution of the compressor, turbine, recuperator and receiver to the total entropy generation rate.

### 5.2.3 Conclusion of the validation

From the validation, it can be concluded that an optimum pressure ratio exists for a system with a set of constants describing the losses in the system. The net power output of the system is

accurately described in terms of the total entropy generation of the system when comparing the first and second laws of thermodynamics. In the next section, the results are shown from the analysis as described in Chapters 3 and 4. In this full analysis, the pressure ratio was treated as a parameter, the mass flow rate and compressor and turbine efficiencies depended on the micro-turbine used while the pressure losses, temperature losses and recuperator efficiency depended on the geometry of the receiver and recuperator.

## 5.3 Results of the full analysis

### 5.3.1 Introduction

Table 5.2 Constants used for the analysis.

Surroundings at location	Value	Unit
$T_0$	300	K
$I$	1 000	W/m <sup>2</sup>
$w$	1 (no wind)	
$P_1$ or $P_{atm}$	80	kPa
<b>Concentrator and receiver</b>		
$e_p$	6.7 (0.38°)	mrad
$\varphi_{rim}$	45	degrees
$refl$	0.93	
$T_{s,max}$	1 200	K
$\beta$	90	degrees
$CR_{min}$	100	-
<b>Recuperator</b>		
$t$	0.001	m
$k$	401	W/mK
$H$	1	m
$L_{max}$	radius of dish concentrator	m

In this section, the results of the optimum recuperator and solar receiver geometry variables are shown. The results also show the optimum operating conditions of the micro-turbines (or points of highest maximum net power output). The results are shown for different concentrator sizes of

$D = 6, 8, 10, 12, 14, 16$  and  $18$  m. For each concentrator diameter, each micro-turbine and each of its operating conditions, the maximum net power output was found. Two cavity receiver models were analysed and results showed no major difference between the maximum net power outputs and optimum recuperator geometry of the two models. However, each receiver construction method had its own optimum geometry. In the remaining sections, the results shown are relevant for the receiver constructed using a circular tube or rectangular channel, except where the cavity construction method is specifically mentioned. The maximum net power output obtained using entropy generation minimisation, is compared with the maximum net power output calculated with the first law of thermodynamics. The results were obtained using the constants in Table 5.2, as explained in Section 3.9.

The constants in Table 5.2 were also changed to see what their effect would be on the maximum net power output and optimum geometry of the system. This means that the effect of surrounding and parameter changes on the maximum net power output and its optimum system geometry required was investigated. These results are also shown. Recommendations for further work are also given.

### 5.3.2 Optimum geometry for maximum net power output

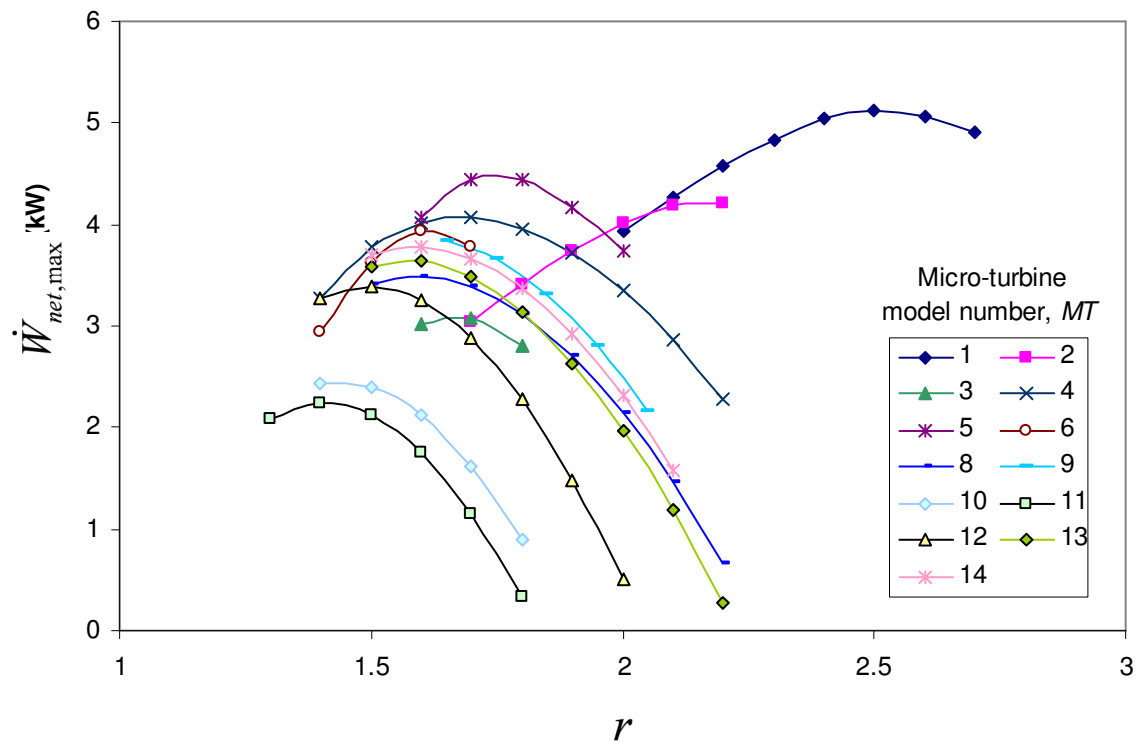


Figure 5.8 Data points for maximum net power output with an optimum geometry for concentrator with  $D = 6$  m.

The analysis found the optimum geometry variables, which produce maximum net power output for the system, at the different parameters. These parameters are the concentrator diameter, micro-turbine used and the operating condition (pressure ratio or mass flow rate) in the range of the specific micro-turbine's optimum compressor efficiency (as shown in Section 3.5.2). Figure 5.8 shows the maximum net power output as a function of the pressure ratio for a collector with a concentrator diameter of  $D = 6$  m as an example. It is very important to note that each data point is a result of the optimisation algorithm and shows a maximum net power output because of its optimised geometry. One should also note that each micro-turbine has an optimum operating point, which produces the highest maximum net power output for the system. The details of the different micro-turbine models are shown in Appendix D. The micro-turbine model number ( $MT$ ) is used to describe a micro-turbine.

**Table 5.3 Results showing optimised geometry variables and maximum net power output for  $MT = 4$  and  $D = 6$  m using a circular tube as receiver construction method, all geometry units in metre, except for the ratios.**

$r$	$\dot{m}$ (kg/s)	$(D_{h,rec})_{opt}$	$(L_{rec})_{opt}$	$(a/b_{rec})_{opt}$	$(D_{h,reg})_{opt}$	$(L_{reg})_{opt}$	$(a/b_{reg})_{opt}$	$(\dot{W}_{net})_{max}$ (W)
1.4	0.083	0.1098	20.61	-	0.008039	3	5.452	3265
1.5	0.089	0.1098	20.60	-	0.006389	3	6.396	3776
1.6	0.096	0.1098	20.60	-	0.005365	3	7.379	4019
1.7	0.102	0.1008	18.91	-	0.005085	3	8.127	4070
1.8	0.109	0.0995	18.67	-	0.004872	3	8.871	3961
1.9	0.115	0.0981	18.40	-	0.004715	3	9.592	3715
2	0.122	0.0956	17.94	-	0.004600	3	10.30	3343
2.1	0.128	0.0901	16.91	-	0.004525	3	10.99	2858
2.2	0.134	0.0877	16.45	-	0.004487	3	11.64	2269

**Table 5.4 Results showing optimised geometry variables and maximum net power output for  $MT = 4$  and  $D = 6$  m using a rectangular channel as receiver construction method, all geometry units in metre, except for ratios.**

$r$	$\dot{m}$ (kg/s)	$(D_{h,rec})_{opt}$	$(L_{rec})_{opt}$	$(a/b_{rec})_{opt}$	$(D_{h,reg})_{opt}$	$(L_{reg})_{opt}$	$(a/b_{reg})_{opt}$	$(\dot{W}_{net})_{max}$ (W)
1.4	0.083	0.0741	12.03	4.071	0.008198	3	5.418	3235
1.5	0.089	0.0916	14.11	2.5	0.006581	3	6.331	3770
1.6	0.096	0.0842	9.892	2.5	0.005782	3	7.186	4085
1.7	0.102	0.0825	7.039	2.5	0.005255	3	8.025	4209
1.8	0.109	0.0743	6.100	2.5	0.004851	3	8.883	4120
1.9	0.115	0.0719	5.897	2.5	0.004693	3	9.610	3881
2	0.122	0.0698	5.731	2.5	0.004578	3	10.32	3514
2.1	0.128	0.0683	5.605	2.5	0.004501	3	11.01	3033
2.2	0.134	0.0671	5.506	2.5	0.004462	3	11.67	2447

The data points (as shown in Figure 5.8) of micro-turbine 4 with  $D = 6$  m and circular tube receiver construction method are shown in Table 5.3. Table 5.4 shows the same data points but a rectangular flow channel (plate) is used as receiver construction method. Take note that the

highest maximum net power output (or optimum operating condition of the micro-turbine) is highlighted for each of these cases.

No significant difference was found between the maximum net power outputs of the different receiver construction methods. However, each receiver construction method had its own optimum geometry. The optimum geometries shown in the tables will be explained in the following section. The remaining results are for both receiver cavity construction methods, except where a specific one is mentioned. Figure 5.9 shows the same results as in Figure 5.8, but as a function of the mass flow rate.

Data points were found for all the concentrator diameters ( $D = 6 - 18$  m) with all the micro-turbines (1 – 45), which gave a reasonable net power output. Figure 5.10 shows the results for  $D = 10$  m and Figure 5.11 shows the results for  $D = 14$  m as a function of the system mass flow rate. When comparing Figures 5.9, 5.10 and 5.11, it can be concluded that the larger micro-turbines performed better at larger concentrator diameters and vice versa. Figure 5.12 shows all the data points found in the analysis for each of the different concentrator diameters, micro-turbines and micro-turbine operating conditions.

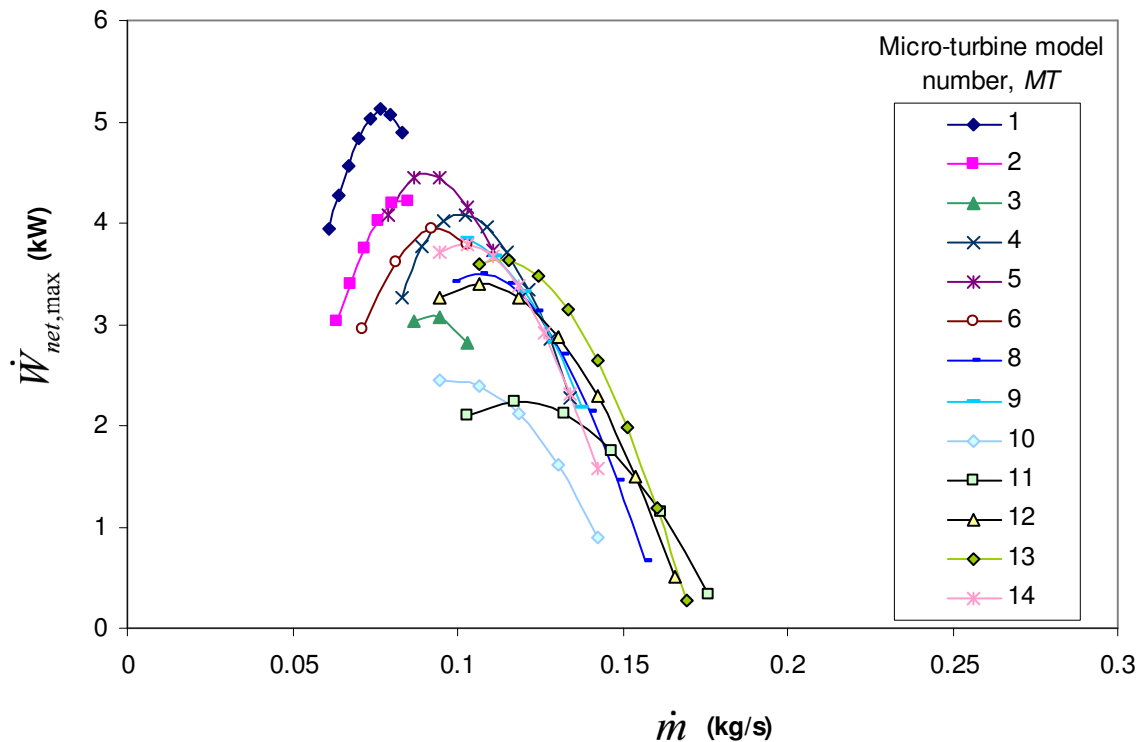


Figure 5.9 Maximum net power output at an optimum geometry for a concentrator with  $D = 6$  m.

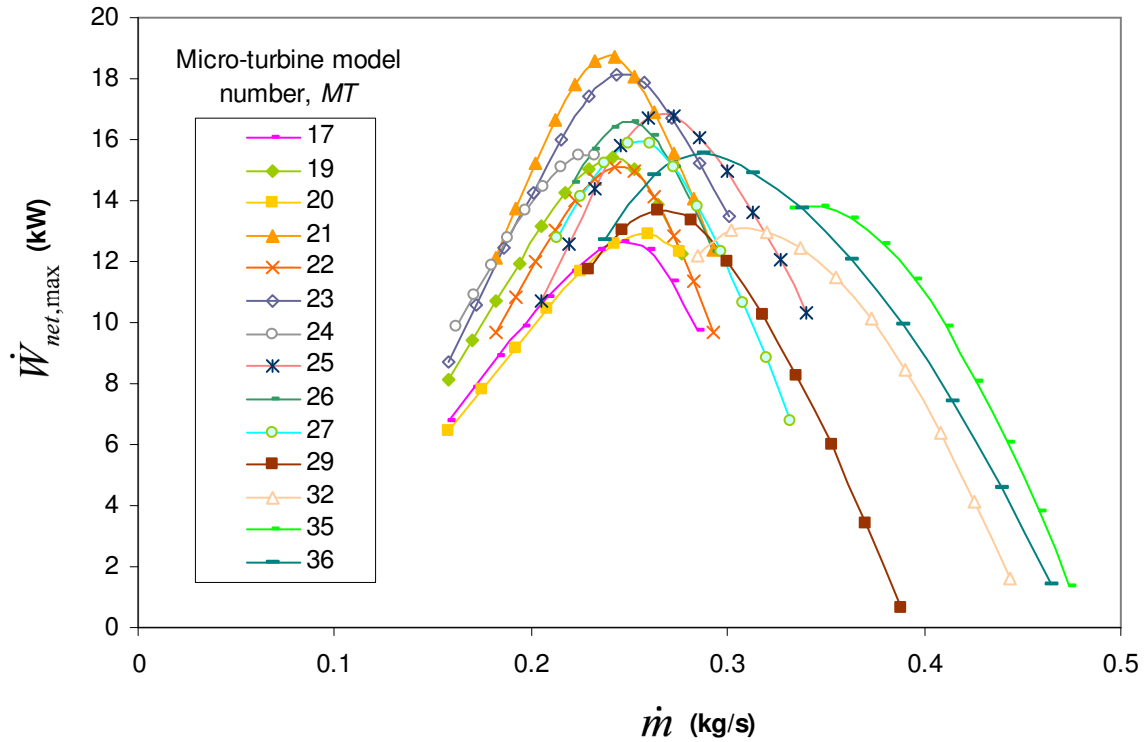


Figure 5.10 Maximum net power output at an optimum geometry for a concentrator with  $D = 10$  m.

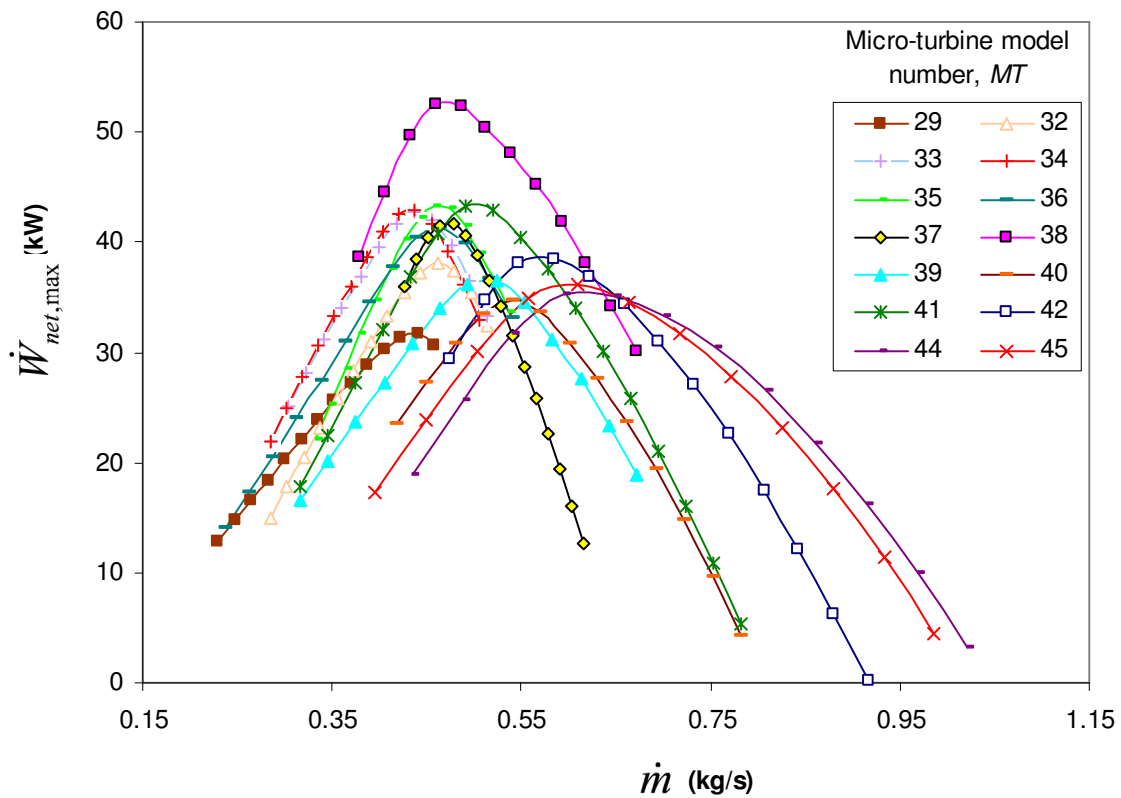


Figure 5.11 Maximum net power output for different micro-turbines and their operating ranges for  $D = 14$  m.

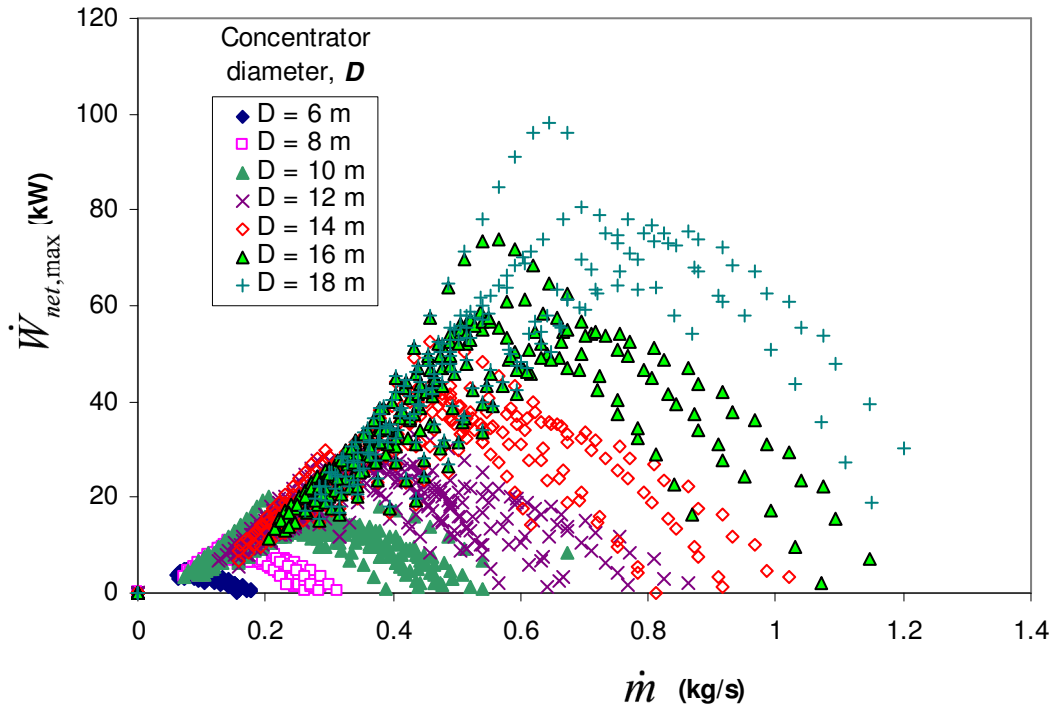


Figure 5.12 All the data points for the range of concentrator diameters and micro-turbines.

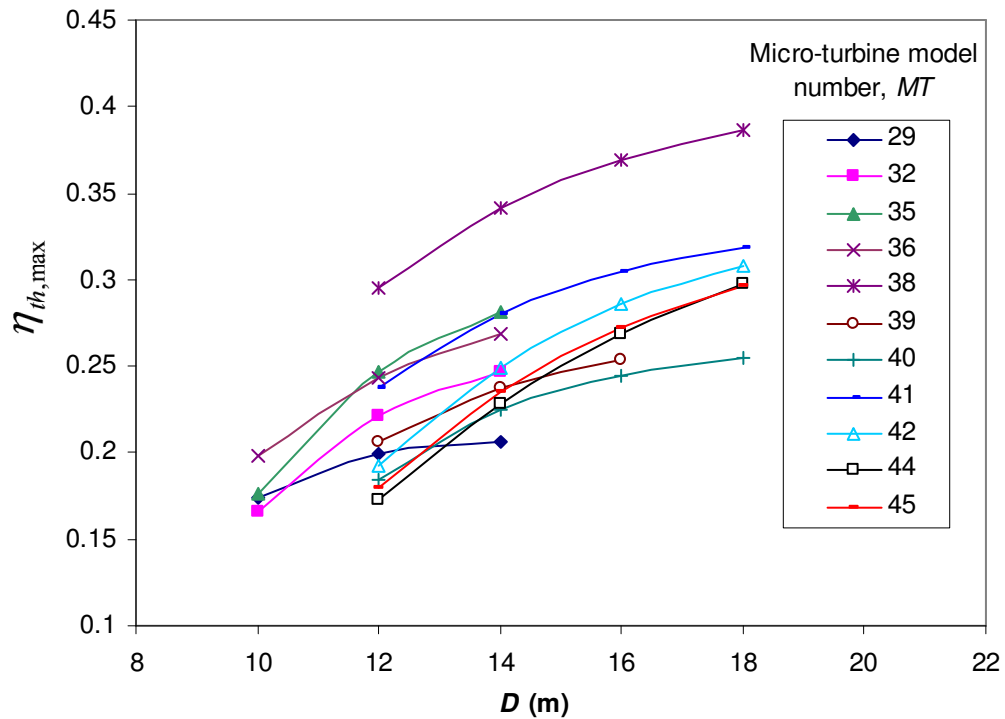


Figure 5.13 Thermal efficiencies of the optimised systems as a function of concentrator diameter and micro-turbine choice.



In some cases, a single micro-turbine had an optimum operating condition (or highest maximum net power output) at a number of different concentrator diameters. This is shown in Figure 5.13, where the maximum thermal efficiencies for each of these optimum points are compared. The thermal efficiency is a function of the concentrator diameter and micro-turbine used. A higher thermal efficiency can be expected when using a larger concentrator, although an even higher thermal efficiency can result when using the correct micro-turbine.

Consider again the data points which give the highest maximum net power output. The optimum recuperator channel aspect ratio of these data points,  $(a/b)_{reg,opt}$ , as a function of the mass flow rate, is shown in Figure 5.14. The relationship between the optimum aspect ratio as a function of the mass flow rate is a linear relationship. This line can be approximated with equation 5.12. Furthermore, when plotting the optimum recuperator channel width as a function of the mass flow rate, a linear relationship is found again.

$$(a/b)_{reg,opt} \approx 83.3\dot{m}_{opt} \tag{5.12}$$

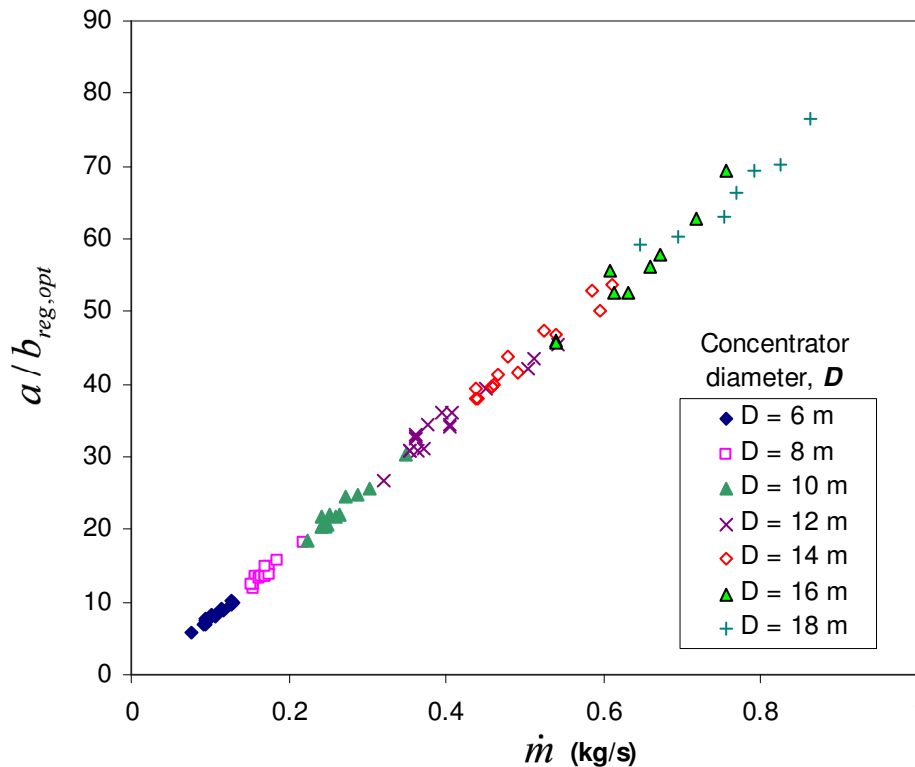


Figure 5.14 Optimum aspect ratio of the recuperator channels at optimum operating conditions of various micro-turbines.

Take note that these data points are the points of the optimum operating conditions for different micro-turbines and different concentrator diameters. When including all of the data points from the analysis, this linear relationship disappears underneath a scattering of data. The linear relationship is thus only valid for an optimised geometry at the optimum operating conditions (with highest maximum net power output) of different micro-turbines. Other studies have found that, for a rectangular channel, an aspect ratio of eight should be used for minimum entropy generation in the channel (Ratts and Raut, 2004). In this work, however, results show that an aspect ratio of eight is not necessarily the optimum aspect ratio for the receiver and recuperator channels in a system which should produce maximum net power output. This is because EGM was done for the whole system, instead of for the components individually.

Figure 5.15 shows that, for a specific micro-turbine (number 27 in this example), there exists a line of maximum net power output as a function of mass flow rate. This is shown more clearly in Figure 5.16 for micro-turbine 41. The larger the concentrator, the more the net power output tends towards this line. The smaller the concentrator diameter and the higher the mass flow rate, the lower maximum net power output can be expected.

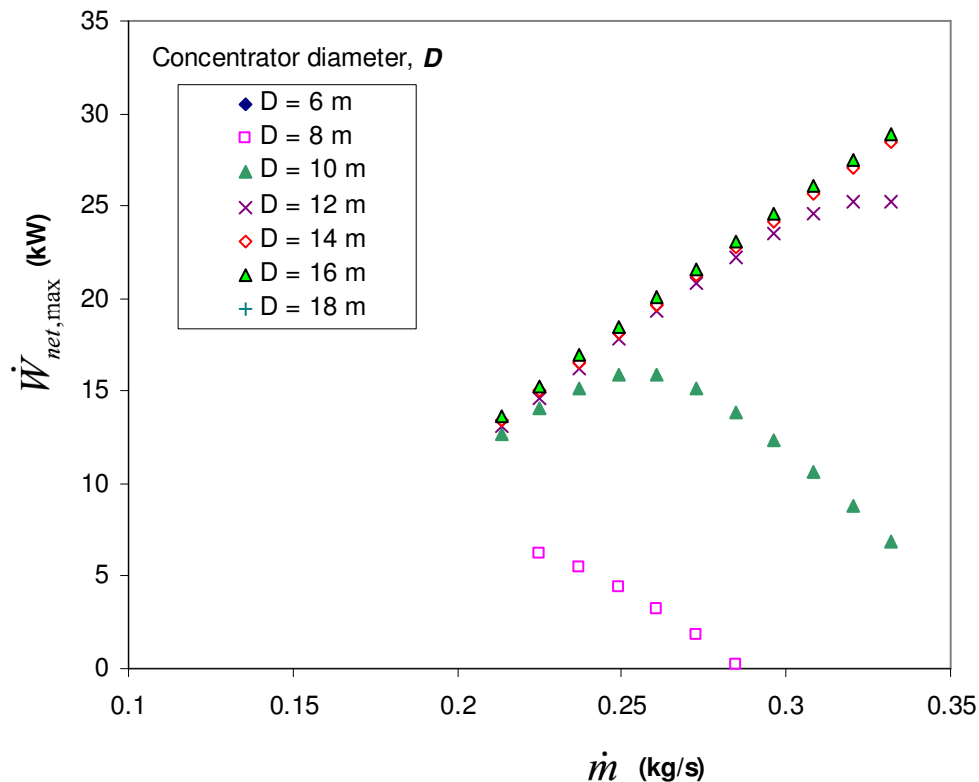


Figure 5.15 Roofline for the maximum net power output for micro-turbine number 27.

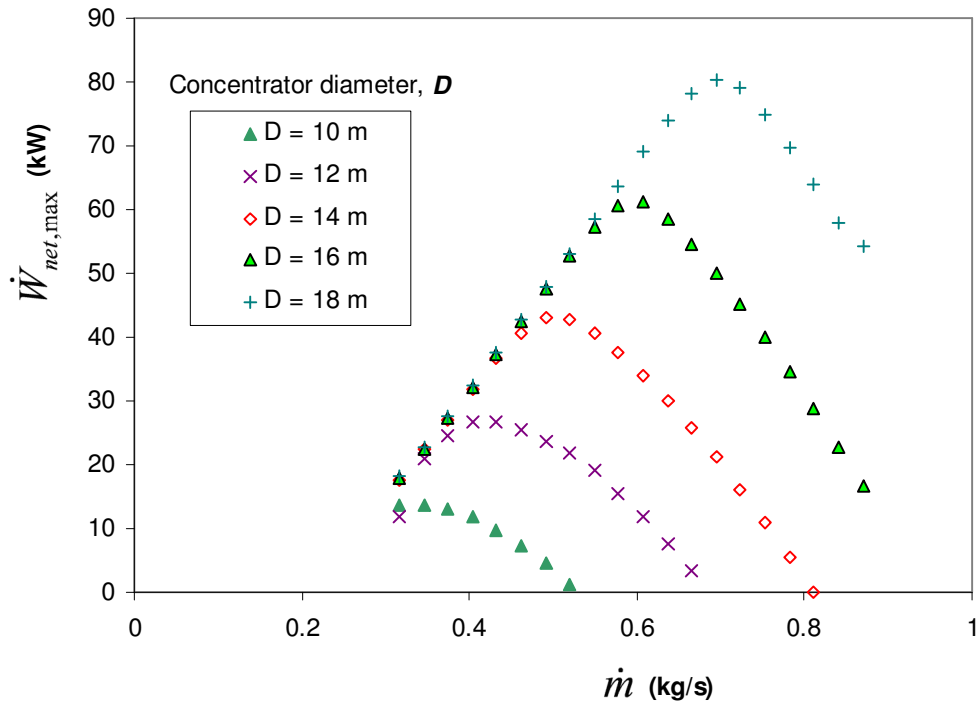


Figure 5.16 Roofline for the maximum net power output for micro-turbine number 41 with different concentrator diameters.

All the data points (where a plate cavity receiver construction method was used) which were geometrically optimised in this analysis, converged to one of two constraint limits. Results showed that a large cavity aperture or small aspect ratio but not necessarily both, is beneficial for the rectangular receiver channel. The two constraints were  $CR \geq 100$  and  $a/b_{rec} \geq 2.5$ . When considering the circular tube receiver construction method, it is interesting to note that most of these optima also lie on an aperture size constraint of  $CR = CR_{min} = 100$ . One can come to the conclusion that it is beneficial for the system's net power output, that the receiver aperture is relatively large in comparison with the concentrator. This can be expected since the effect of wind was neglected.

The optimum recuperator length,  $L_{reg,opt}$ , mostly converged on its constraint, as was set in Section 3.8. This is shown in Figure 5.17, where all the data points are shown, and in Figure 5.18, where the optimum recuperator length is shown for micro-turbine 41 at  $D = 16$  m. The optimum recuperator length increased as the mass flow rate increased until the constraint was reached. It is therefore more beneficial for a system with small mass flow rate to have a short recuperator. Systems with short recuperator lengths (relative to the concentrator radius), however, usually do not have high maximum net power outputs.

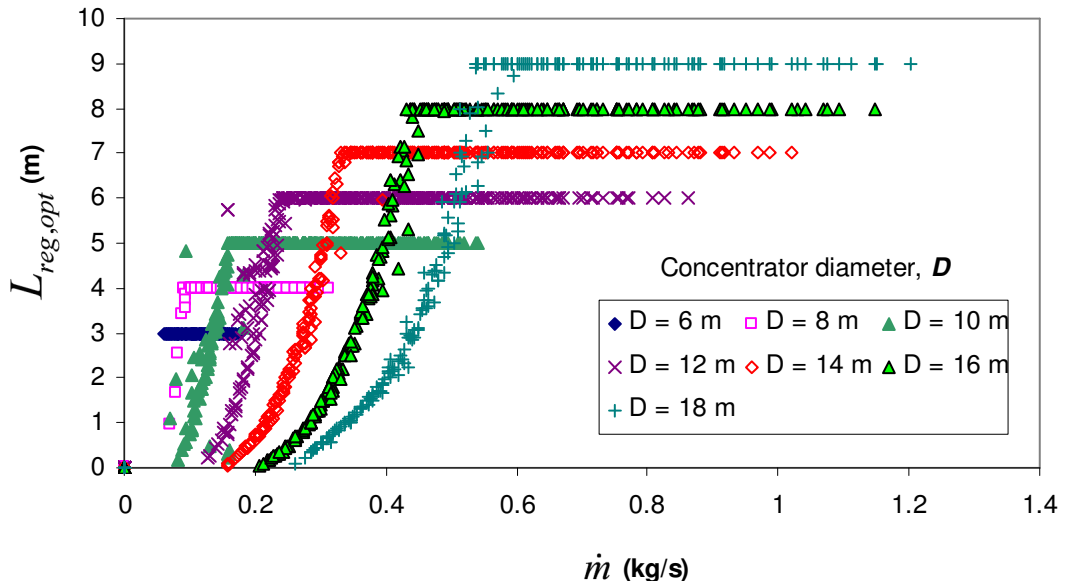


Figure 5.17 Convergence of the optimum recuperator length to its maximum constraint.

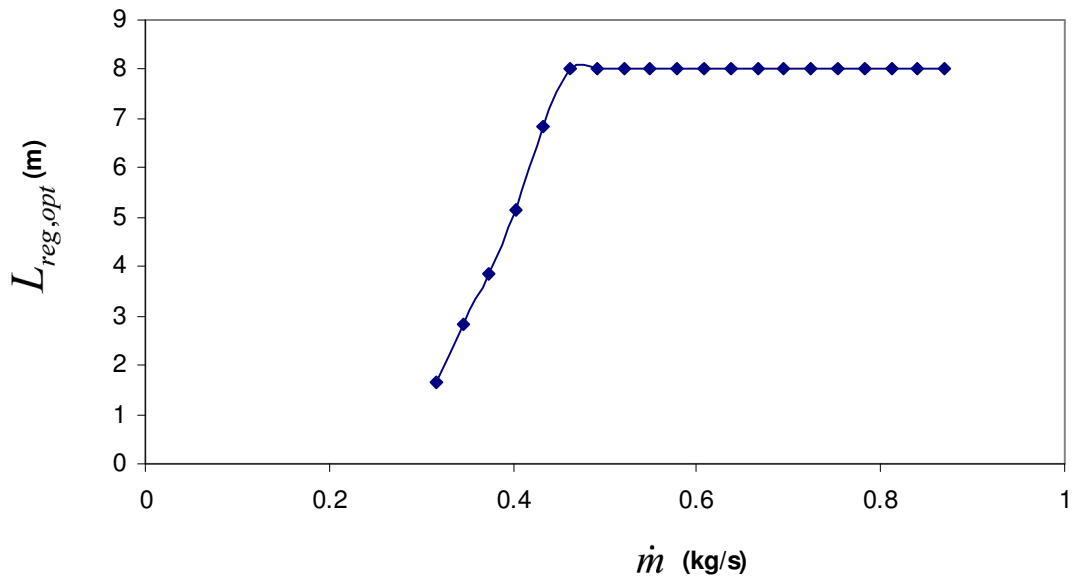


Figure 5.18 Convergence of the optimum recuperator length for  $D = 16$  m with micro-turbine 41.

In Figure 5.19, the optimum hydraulic diameter of the recuperator channels is shown as a function of system mass flow rate. At small mass flow rates, the optimum hydraulic diameter increases as system mass flow rate increases, until the recuperator length constraint is reached. For increasing mass flow rate, the optimum hydraulic diameter decreases until a minimum diameter is reached where the maximum pressure drop exists. The optimum hydraulic diameter increases slightly as the mass flow rate increases.

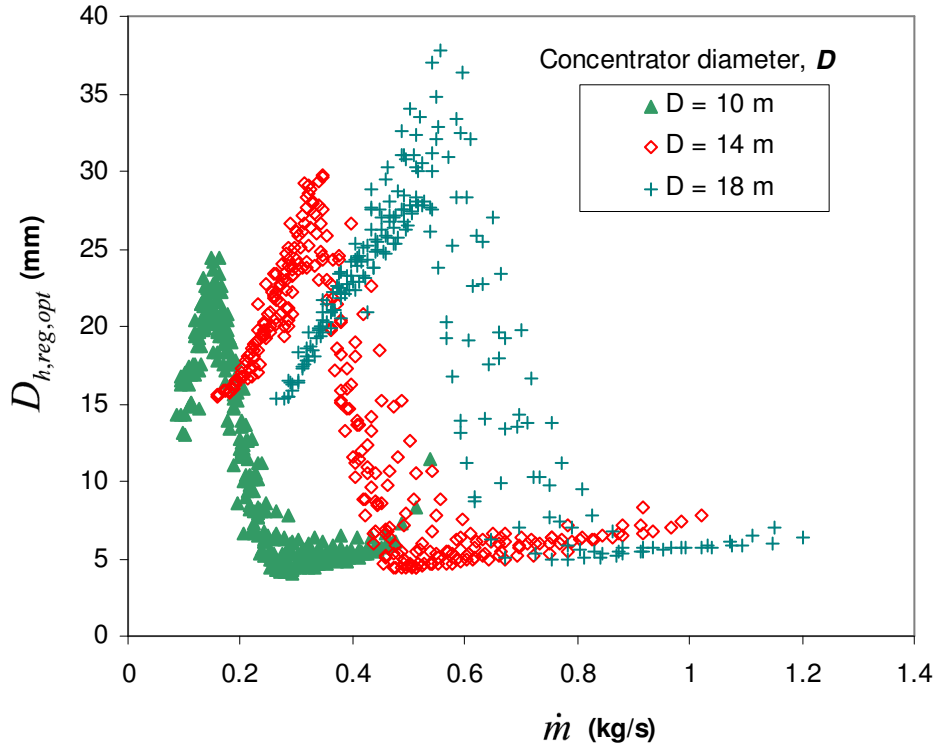


Figure 5.19 Optimum hydraulic diameter of recuperator channels as a function of system mass flow rate for  $D = 10, 14$  and  $18$  m.

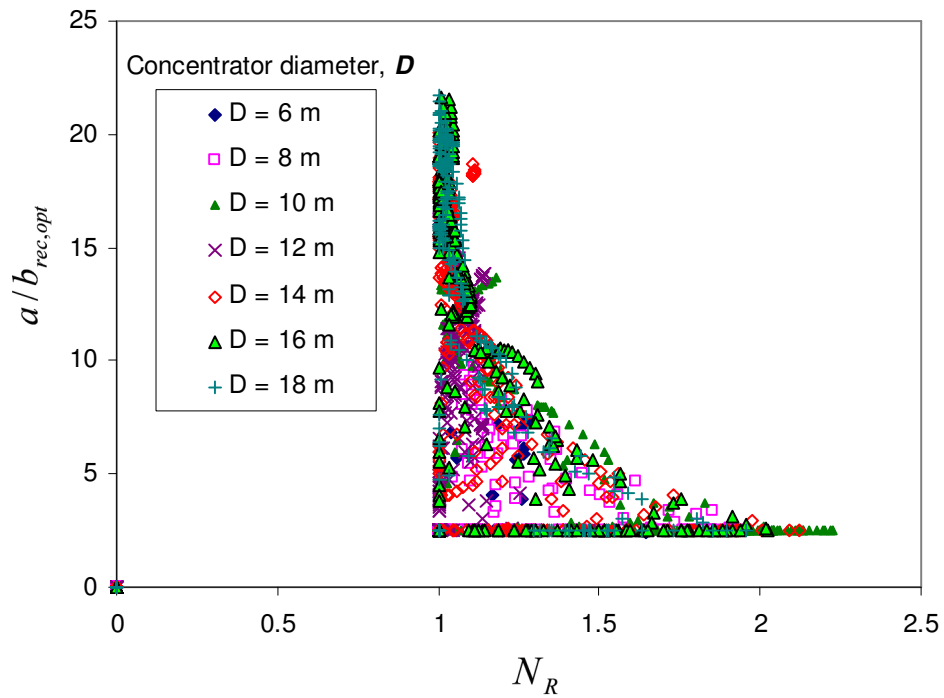


Figure 5.20 Optimum number of rectangular tubes between the receiver edge and the receiver aperture as a function of the optimum receiver channel aspect ratio.

It was also found that the receiver of the optimised system would not necessarily have the aperture diameter that intercepts the maximum solar heat input, as shown in Figure A.4. According to the results, a larger aperture diameter, which absorbs less solar heat (see Appendix A) can produce a larger net power output in some systems. From each of the optimised data points in the analysis, it was found that there exists an optimum number of tube diameters,  $N_D$ , or rectangular channels,  $N_R$ , which fit in between the receiver aperture edge and the receiver edge (in Figure 3.6, for example,  $N_D = 4$ ). The definition of  $N_D$  is shown in equation 5.13.

$$N_D = \left( (\sqrt{3} - 1)d \right) / (2D_{h,rec}) \quad (5.13)$$

For a specific concentrator diameter,  $N_D$  decreases as the mass flow rate increases until it reaches its constraint of two, except for systems using large concentrators with a plate-type receiver. The optimum receiver tube diameter was found to be relatively large compared with the receiver. It was found that, for all the data points in the analysis,  $2 \leq N_D \leq 4$ . This means that the optimum receiver tube diameter is mostly relatively large. For the rectangular channel receiver,  $D_{h,rec}$  in equation 5.12 can be replaced with  $a$  – the longest side of the rectangular channel. For all the optimised plate-type receiver geometries in the analysis, it was found that  $1 \leq N_R \leq 2.3$ . For the rectangular channel receiver at large concentrators,  $N_R$  did not decrease as the mass flow rate increased, but for small concentrators, it behaved similarly to the circular tube receiver. Figure 5.20 shows that, for an optimum receiver channel geometry in all of the cases, a large aspect ratio is accompanied with a small  $N_R$  and a large  $N_R$  is accompanied with a small aspect ratio. Note that all the data points are shown in Figure 5.20.

Another interesting observation for the circular tube receiver is the relationship between the optimum receiver diameter,  $D_{rec,opt}$  and the optimum receiver length,  $L_{rec,opt}$ . This is shown in Figure 5.21. It is optimum for a long receiver tube to have a small tube diameter and vice versa, except at very small receiver tube lengths where the tube diameter is also small. For the rectangular channel receiver, however, there is no established pattern between the hydraulic diameter and channel length. This can be expected because the hydraulic diameter of a rectangular channel is a function of the channel aspect ratio.

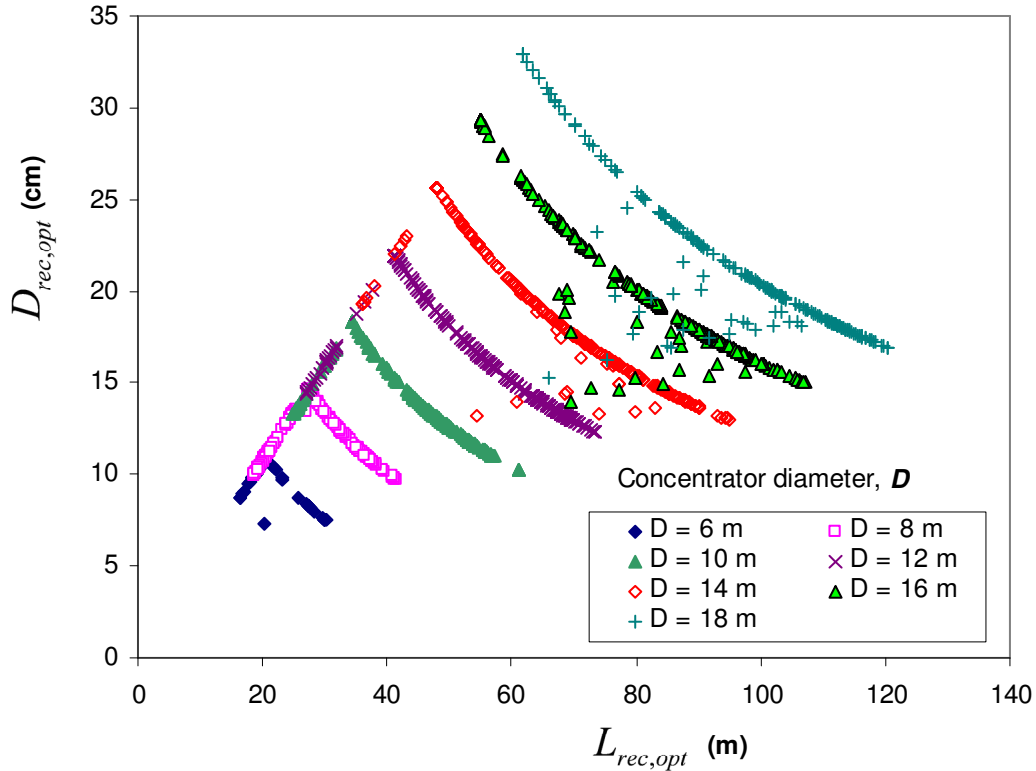


Figure 5.21 Relationship between the optimum tube diameter and the optimum length for the circular tube receiver.

This section showed the optimum recuperator and receiver geometries for a recuperative open and direct solar thermal Brayton system, which produces its maximum net power output, as calculated with the method of entropy generation minimisation.

### 5.3.3 Maximum net power output with optimum operating conditions and system properties

Consider again the constants given in Table 5.2. For all the optimised data points (all  $D$ , and all operating points of all the micro-turbines), the optimum recuperator channel mass flow rate behaved in a specific way relative to the mass flow rate of the system. This is shown in Figure 5.22. The optimum  $NTU$  (see equation 3.31) also behaved in a very specific manner as a function of the system mass flow rate, as shown in Figure 5.23.

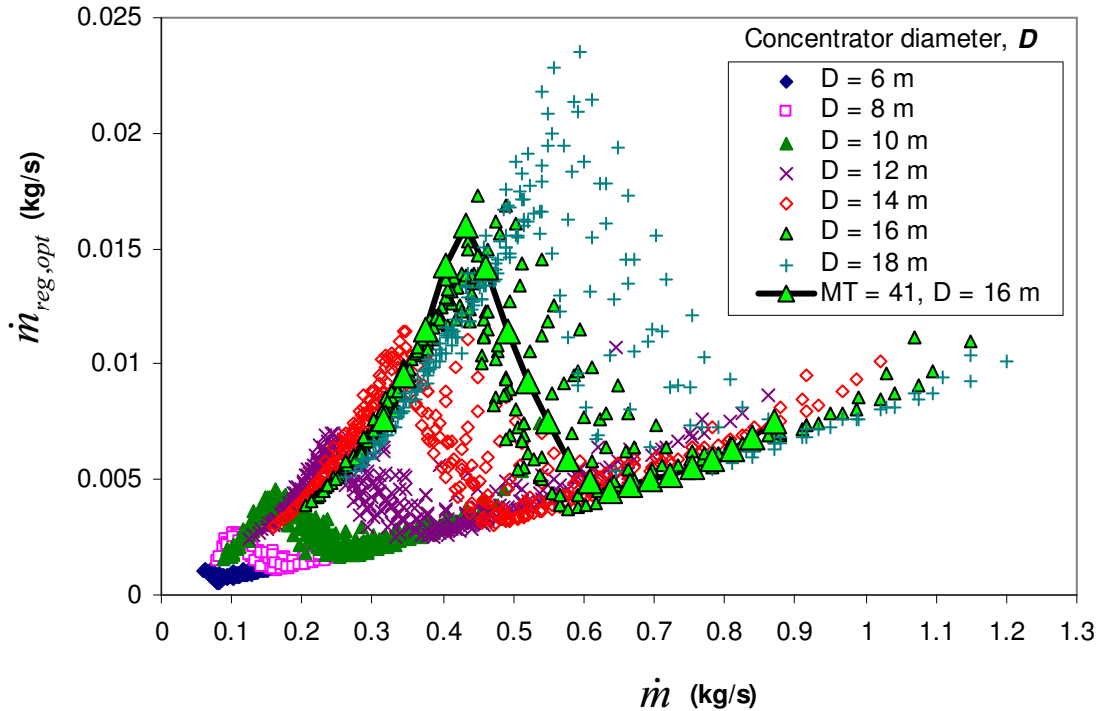


Figure 5.22 Optimum recuperator channel mass flow rate for all data points.

The behaviour of the optimum mass flow rate of the recuperator is shown more clearly in Figure 5.24 (showing only  $D = 8, 12$  and  $16$  m). Note the similarity between Figures 5.24 and 5.19. Take note that each data point in Figure 5.24 has an optimum geometry and gives maximum net power output at its specific mass flow rate. When inspecting Figure 5.25 (again,  $D = 6, 10, 14$  and  $18$  m are not shown, but behaved similarly), it can be concluded that, for all the data points, the optimum  $NTU$  increases as the system mass flow rate increases until it reaches its maximum. This means that it is most beneficial for a system with a small mass flow rate to have a small  $NTU$ . The following paragraph explains why.

Micro-turbine 41 is considered because it has a very large operating range at its maximum compressor efficiency. Understanding the behaviour of this micro-turbine is very helpful in understanding Figures 5.24 and 5.25. The optimum distribution of the minimum entropy generation is shown for  $D = 16$  m with micro-turbine 41 in Figure 5.26. This distribution was found to be similar for all the combinations of concentrator diameters and micro-turbines optimised in this analysis. Note that for the optimised system, the entropy generation in the receiver is the largest (Figure 5.26a).



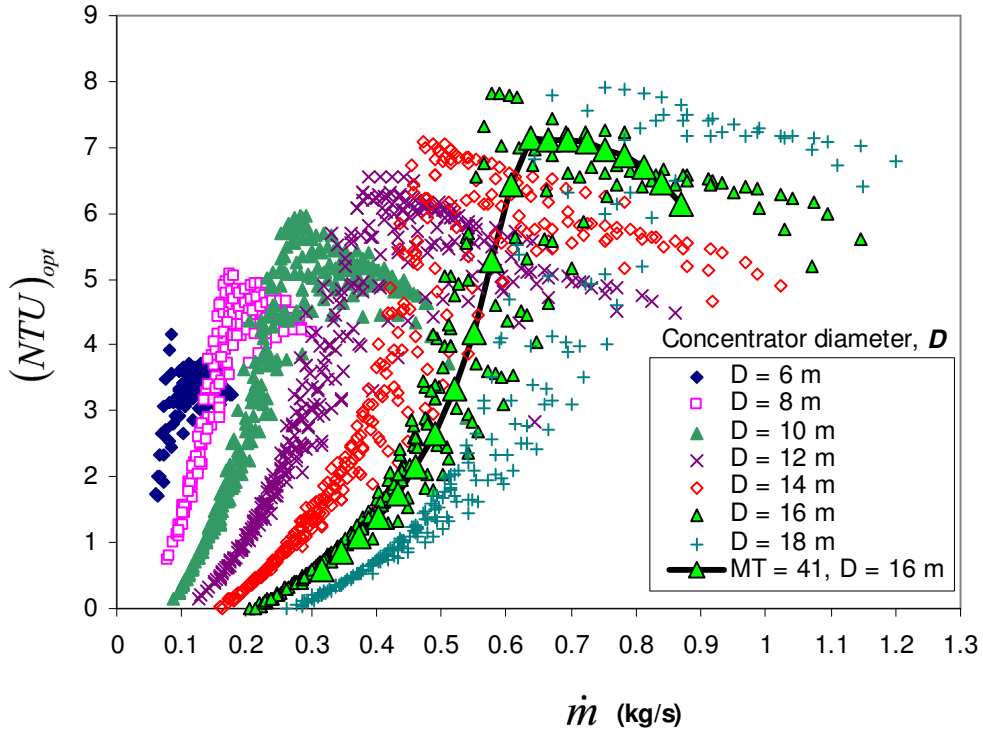


Figure 5.23 Optimum  $NTU$  for all data points.

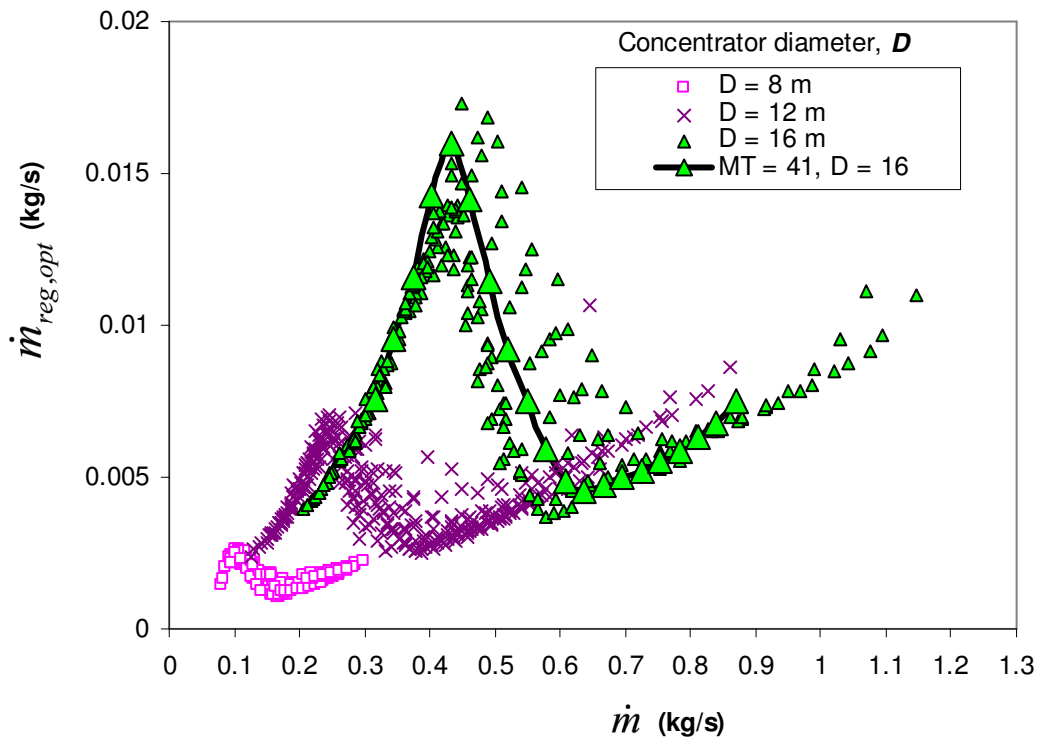


Figure 5.24 Optimum recuperator channel mass flow rate ( $D = 8, 12$  and  $16$  m).

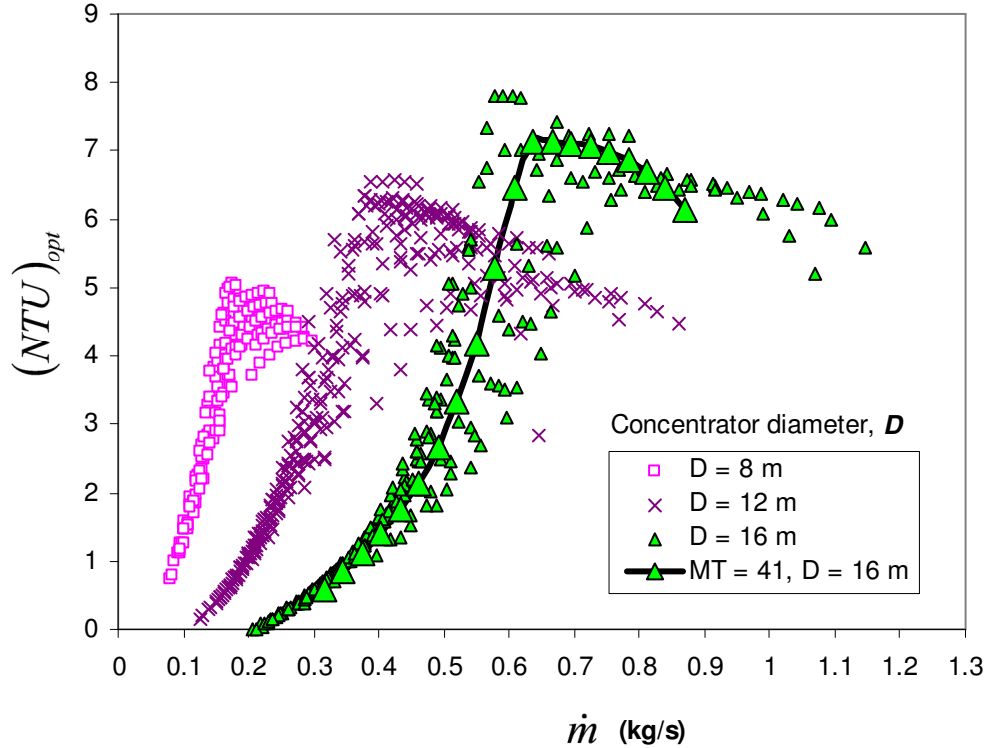


Figure 5.25 Optimum  $NTU$  for all data points ( $D = 8, 12$  and  $16$  m).

Consider the point where the minimum external irreversibility rate,  $\dot{I}_{ext,min}$ , is at its highest (Figure 5.26d).  $\dot{I}_{ext,min}$  seems to be at a maximum when the mass flow rate is small.

$$\dot{I}_{ext} = \dot{m}c_{p0}(T_1 - T_{11}) - \dot{m}T_0c_{p0} \ln\left(\frac{T_1}{T_{11}}\right) \quad (5.14)$$

From equation 5.14 it follows that, for high external irreversibilities,  $T_{11}$  must be high, which means that  $\eta_{reg}$  should be small (see equation 3.57). This is why the optimum  $NTU$  is small at small mass flow rates, as shown in Figure 5.25. The optimum  $NTU$  increases as the mass flow rate increases. The optimised data shows that a small  $NTU$  is established with the use of a small surface area, large hydraulic diameter (Figure 5.19) and large recuperator channel mass flow rate, which increase respectively until the maximum recuperator length constraint is reached (around 0.45 kg/s in Figure 5.24). A large hydraulic diameter also keeps the pressure drop and minimum entropy generation rate due to fluid friction,  $\dot{S}_{gen,int,min,\Delta P}$ , low for the recuperator (Figure 5.26c). After the length constraint is reached (Figures 5.17 and 5.18), the recuperator mass flow rate and hydraulic diameter decrease (Figure 5.19) as the mass flow rate increases to

ensure an increase in  $NTU$  as the system mass flow rate increases. Note that  $\dot{S}_{gen,int,min,\Delta P}$  grows quite big at these mass flow rates because the hydraulic diameter decreases. At these mass flow rates, the high pressure drops can be considered as most beneficial for the net power output of the system.

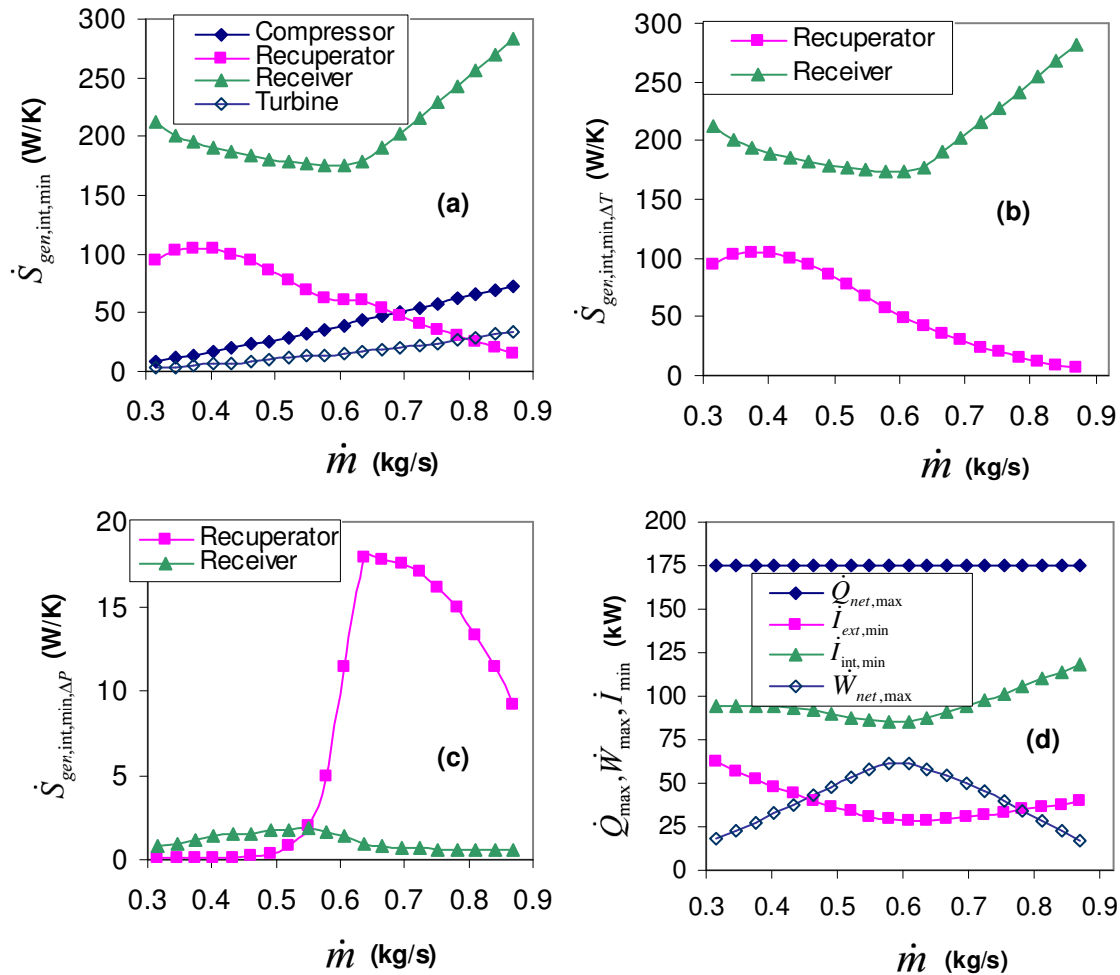
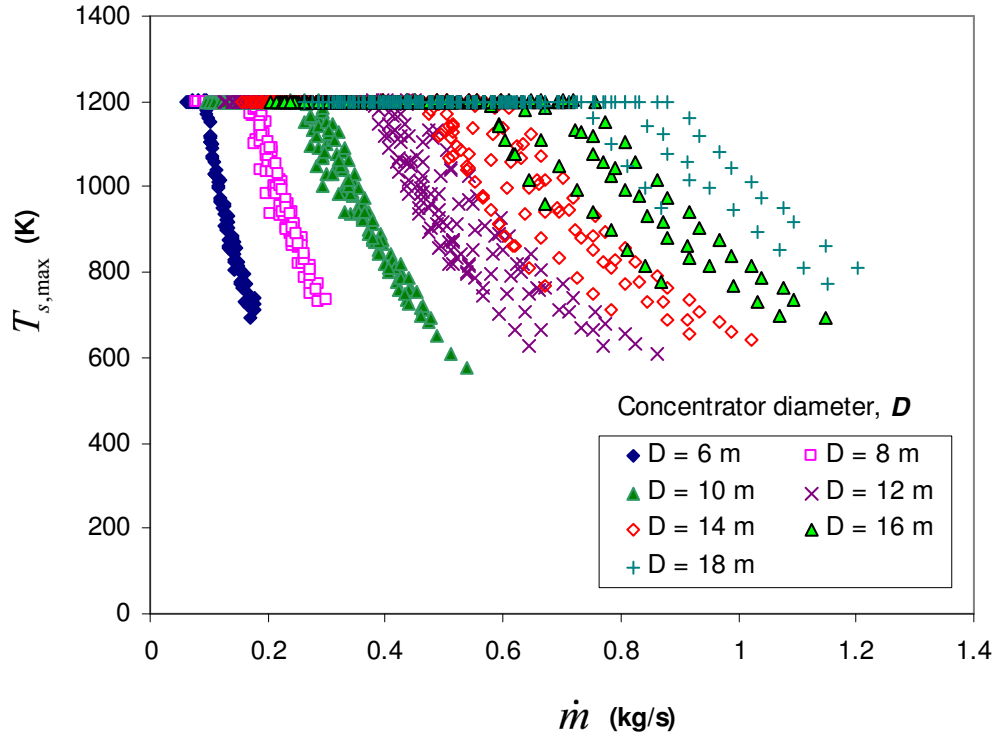


Figure 5.26 Geometry optimised system data points ( $MT = 41$ ,  $D = 16$  m) : (a) – Minimum total internal entropy generation rate; (b) – Contribution to total minimum internal  $\dot{S}_{gen}$  due to temperature difference; (c) – Contribution to minimum internal  $\dot{S}_{gen}$  due to frictional pressure drop; (d) – Minimum irreversibilities and maximum power.

In Figure 5.27 it is shown that the maximum receiver surface temperature of the optimised data stays constant as a function of mass flow rate at small mass flow rates. This is due to the temperature constraint of 1 200 K, as shown in Section 3.8. At higher mass flow rates, the maximum surface temperature of the optimised data decreases as a function of mass flow rate. The larger the concentrator diameter, the larger the mass flow rate at which the maximum surface

temperature would start decreasing. When comparing Figure 5.27 with Figures 2.13 – 2.17, it can be concluded that the operating temperature range of a solar thermal power cycle depends also on the mass flow rate through the receiver and the receiver melting temperature.



**Figure 5.27 Maximum receiver surface temperature of all the optimised data points (all micro-turbines and each of its operating conditions).**

When considering the minimum entropy generation rate in the solar receiver (Figure 5.26a - c), it follows that the receiver performs optimally when  $\dot{S}_{gen,int,min,\Delta P}$  is as small as possible. The largest component of the minimum receiver entropy generation rate should be the temperature difference component,  $\dot{m}c_p \ln(T_6/T_5)$ . The downward minimum entropy generation slope for the receiver at small mass flow rates (Figure 5.26a) is due to an increase in the  $NTU$ , which increases  $T_5$  (see equations 3.58 and 3.59). In the receiver, at small mass flow rates, the optimum  $T_{s,max}$  stays constant as a function of mass flow rate (Figure 5.27), which means that  $\dot{S}_{gen,int,min,\Delta T}$ , due to temperature difference ( $T_6/T_5$ ), decreases as the mass flow rate increases (Figure 5.26b). Eventually, the optimum  $NTU$  reaches its maximum at a high mass flow rate (Figure 5.25). For increasing mass flow rate,  $\dot{S}_{gen,int,min,\Delta T}$  increases as a function of mass flow rate (Figure 5.26b) and the maximum receiver surface temperature of the optimised data decreases (Figure 5.27).

Consider the point where  $\dot{I}_{ext,min}$  is at a minimum (Figure 5.26d).  $T_{11}$  will be at a minimum and the recuperator efficiency will be at a maximum. As  $\dot{I}_{ext,min}$  increases slightly with mass flow rate, the optimum  $NTU$  decreases slightly as shown in Figure 5.25. At the highest optimum  $NTU$  point, the recuperator channel mass flow rate is again utilised to be increased as the system mass flow rate increases in order to keep the optimum  $NTU$  at its maximum. In most of the cases (but not all cases), the highest maximum net power output in the operating range of the micro-turbine was found at a mass flow rate close to the point of highest optimum  $NTU$  or at higher mass flow rates. To keep the optimum  $NTU$  constant, the hydraulic diameter is also kept constant, but increases slightly (Figure 5.19) as the system mass flow rate increases to keep  $\dot{S}_{gen,int,min,\Delta P}$  in the recuperator small. This, in turn, forces the recuperator mass flow rate to also increase slightly as the system mass flow rate increases, as shown in Figure 5.24.

It seems to be more beneficial for the system when  $\dot{S}_{gen,int,min,\Delta T}$  in the receiver is higher at higher mass flow rates. For this reason, there is a decrease in the optimum  $NTU$  (and  $T_5$ ) at high mass flow rates.

Consider Figure 5.26d in more detail and note how the maximum net power output increases as the minimum entropy generation decreases as a function of mass flow rate. The highest maximum net power output is at the point where the minimum entropy generation rate or minimum irreversibility rate ( $\dot{I}_{ext,min} + \dot{I}_{int,min}$ ) is the lowest.

Figure 5.28 shows the optimum performance of the system in terms of the optimum pressure drop in the receiver and recuperator, as a function of mass flow rate, for micro-turbine 41 with  $D = 16$  m. It is interesting to note that, for optimum systems, the pressure drop of the receiver is larger than the pressure drop in the recuperator when the mass flow rate is small. This changes at a specific mass flow rate, whereafter it is optimal for the recuperator pressure drop to be larger than the receiver pressure drop. This change is due to a decreased hydraulic diameter, as was found from Figure 5.26. Note how Figure 5.28 relates to  $\dot{S}_{gen,int,min,\Delta P}$  in Figure 5.26c. Exactly the same behaviour was found for the other micro-turbines with  $D = 16$  m.

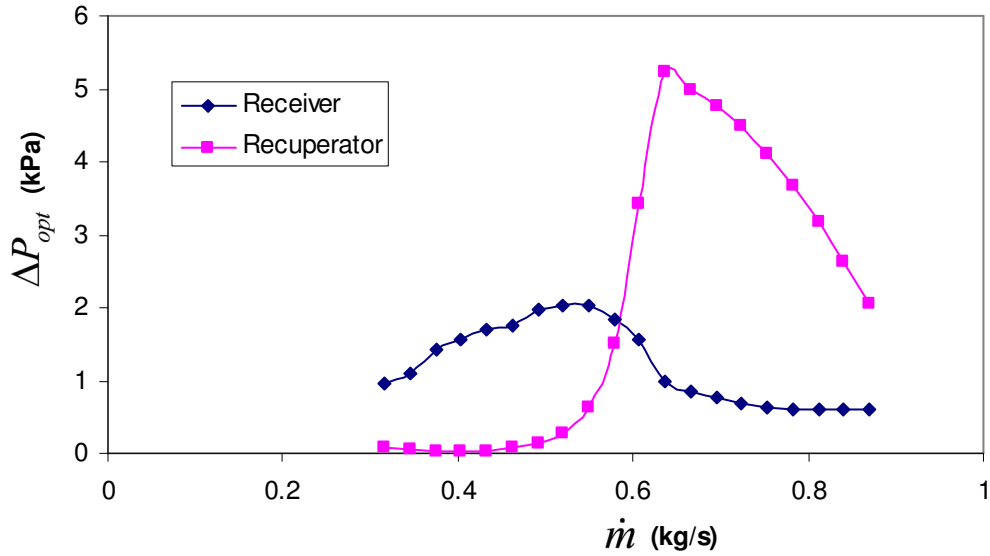


Figure 5.28 Optimum pressure drop in receiver and recuperator channel for micro-turbine 41 and  $D = 16$  m.

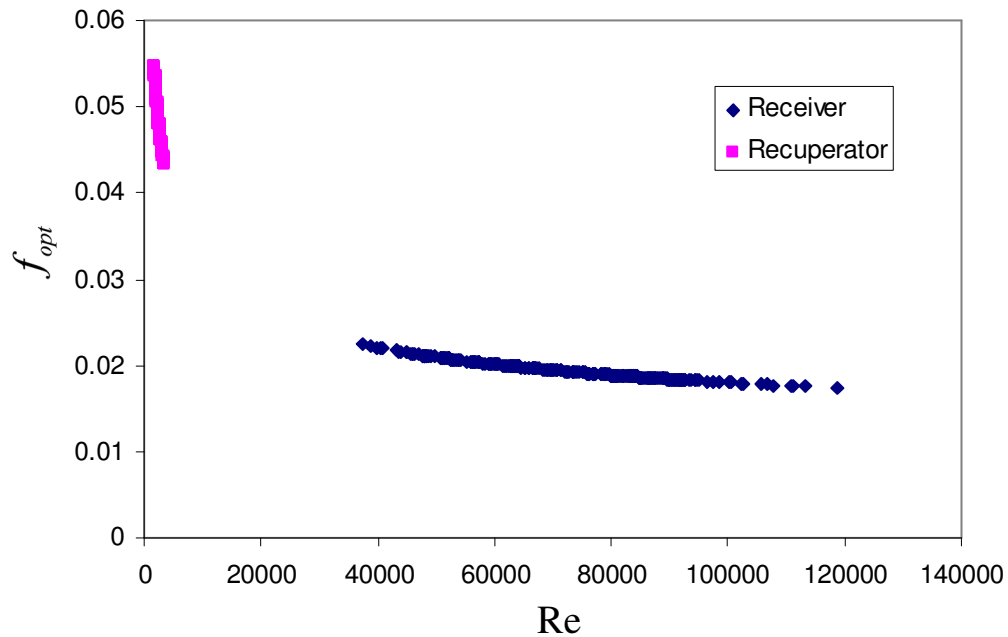


Figure 5.29 Optimum friction factor in receiver and recuperator for  $D = 16$  m.

The optimum friction factor of the receiver and recuperator channels, as a function of Reynolds number, is shown in Figure 5.29 for systems with different micro-turbines and operating mass flow rates with  $D = 16$  m. It is optimum for the recuperator to operate in the laminar flow regime while the receiver operates in the turbulent flow regime. From Figure 5.30, this can also be concluded for all systems analysed in this study. Figure 5.30 shows the optimum range of friction factors as a function of mass flow rate for all the data points. The optimum receiver friction factor decreases as a function of system mass flow rate or Reynolds number. For the large concentrator

diameters, the optimum recuperator friction factor increases with system mass flow rate until it reaches a maximum whereafter it slowly decreases with system mass flow rate. It is more beneficial for recuperators in systems with large concentrators to have a smaller friction factor when the system mass flow rate is small.

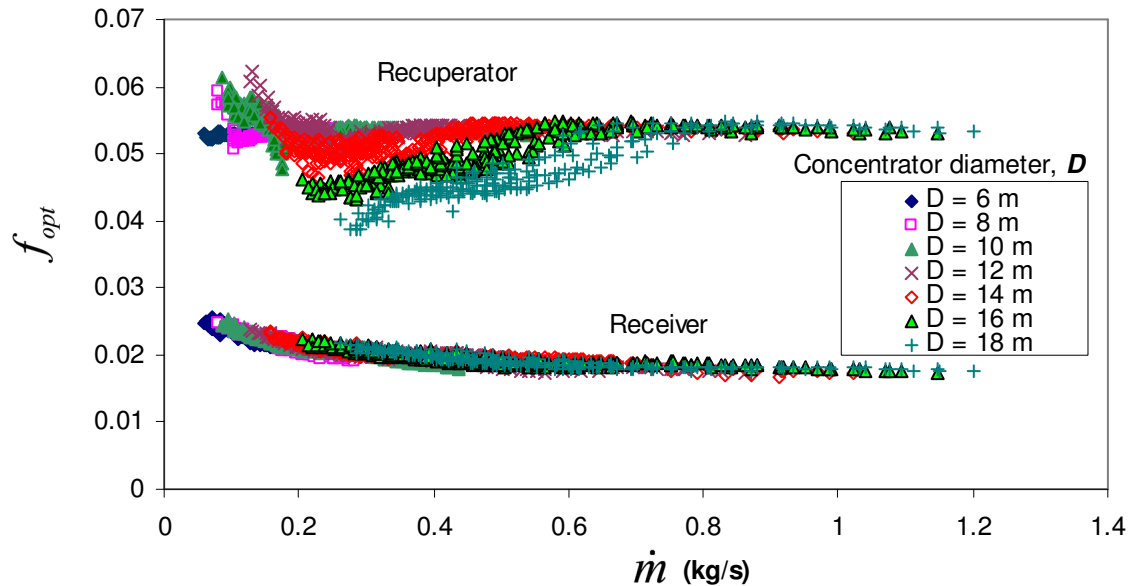


Figure 5.30 Optimum friction factor for all data points.

Figure 5.31 reveals that there exist linear relationships between the optimum recuperator efficiency and the optimum recuperator channel hydraulic diameter. Note that only the data points which gave the highest maximum net power output of a micro-turbine are shown. For small concentrator diameters, the optimum recuperator efficiency is smaller compared with the optimum recuperator efficiency required for larger concentrator diameters. When the optimum recuperator channel hydraulic diameter is large, it is more beneficial for the system that the recuperator efficiency is smaller. This can be compared with the results shown in Figures 5.25 and 5.26c where a high optimum  $NTU$  is accompanied with a large pressure drop or small hydraulic diameter.

Figure 5.32 shows that there exists an optimum ratio of system mass flow rate to recuperator channel mass flow rate. Again, only the data points with highest maximum net power output are shown. When comparing these results with the results from Figure 5.24, one finds that this line (Figure 5.32) falls on the third section of optimum system behaviour (or close to the mass flow rate with the highest  $NTU$  or at higher mass flow rates). This optimum linear ratio seems to have a slope close to 0.01. The result is shown in equation 5.15.

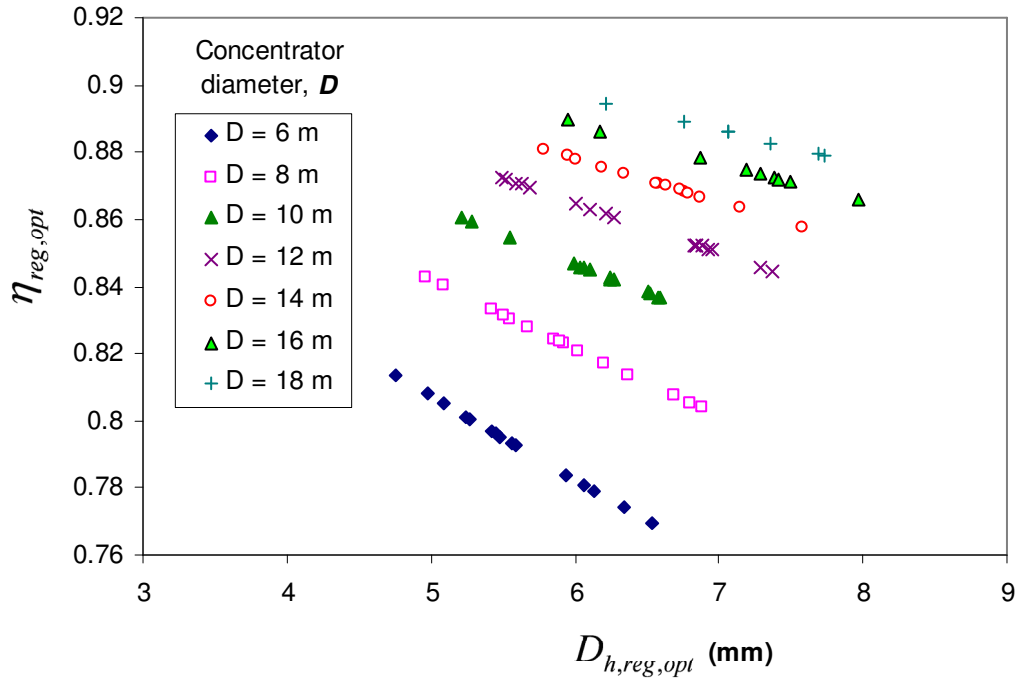


Figure 5.31 Linear relationship between optimum recuperator efficiency and channel hydraulic diameter.

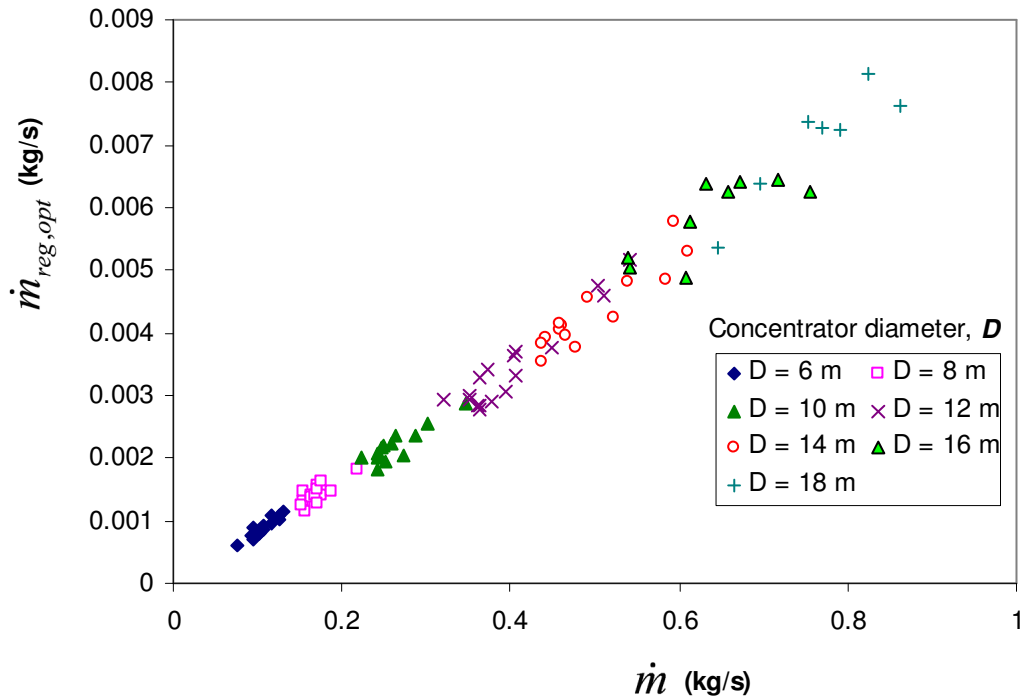
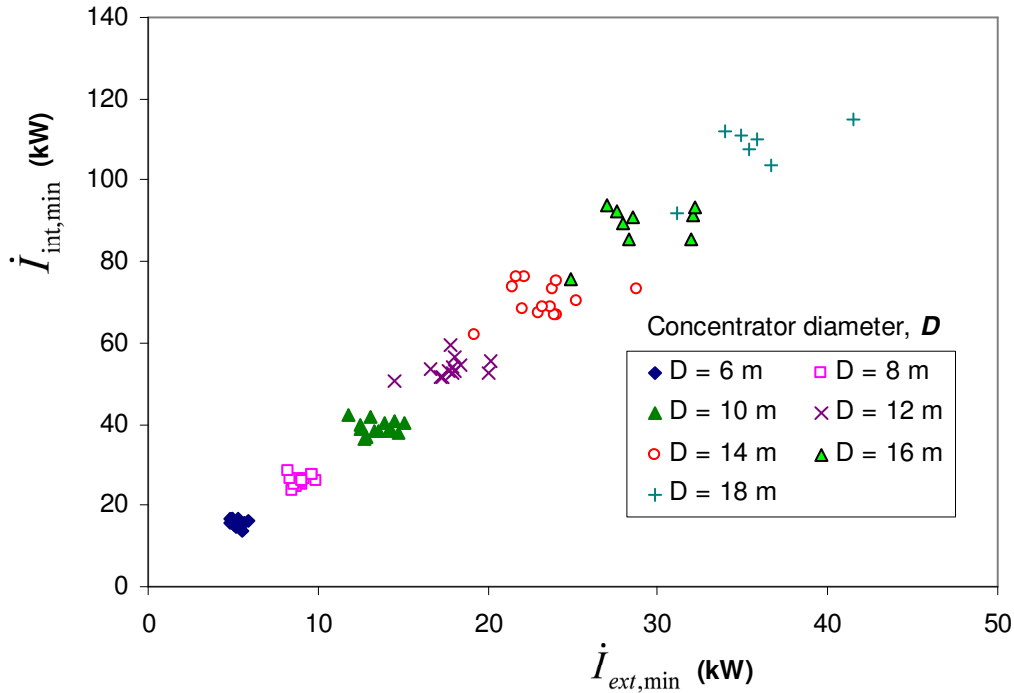


Figure 5.32 Linear relationship between optimum recuperator channel mass flow rate and optimum system mass flow rate.



$$\dot{m}_{opt} \approx 115\dot{m}_{reg,opt} \quad (5.15)$$

Figure 5.33 shows that there exists a relationship between the minimum internal and external irreversibilities of the system, when the data points with highest maximum net power output are considered.



**Figure 5.33 Minimum internal system irreversibility rate as a function of minimum external system irreversibility rate for maximum system net power output.**

From Figure 5.33, it follows that the largest maximum net power output for a system (or optimum operating point) is at a point where the internal irreversibility rate is approximately three times larger than the external irreversibility rate. This result can be approximated with equation 5.16 for all optimisation results in this analysis (with different concentrators and micro-turbines) where an optimum operating condition was found:

$$-T_0 [\dot{S}_{gen}]_{int,min} \approx C_W [\dot{m}c_{p0}(T_1 - T_{11}) - \dot{m}T_0 c_{p0} \ln(T_1 / T_{11})]_{ext,min} \quad (5.16)$$

where  $C_W = \dot{I}_{int,min} / \dot{I}_{ext,min} \approx 3$ .

Figure 5.34 shows that  $C_W$  mostly increases as the system mass flow rate increases. The rate of increase decreases as the concentrator diameter increases. Figure 5.34 shows that  $2.4 \leq C_W \leq 4$ , depending on the mass flow rate and concentrator diameter. Other data points which are not at an optimum operating point (or highest maximum net power output), or close to one, do not fall in this range.

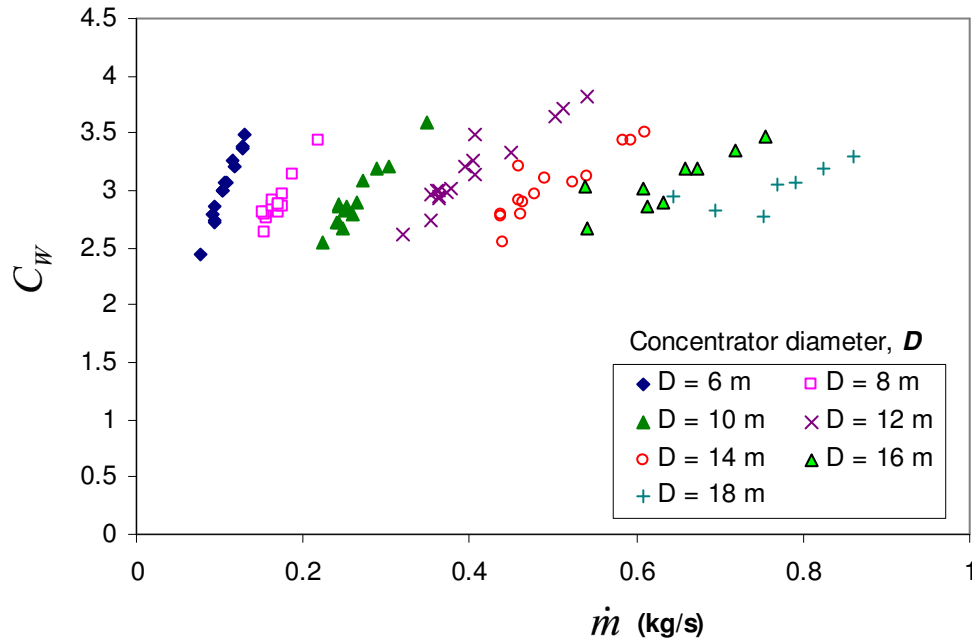


Figure 5.34  $C_W$  as a function of the system mass flow rate.

The results shown in the previous two sections can be considered in the preliminary stages of the design of an open and direct solar thermal Brayton cycle.

### 5.3.4. Comparison of second and first law results

The net power output for the solar thermal Brayton cycle can also be calculated with the first law of thermodynamics together with the temperatures and pressures of the system, as described in Section 3.6. Equation 5.17 can be used to compare the net power output in terms of the first law with the net power output described in terms of the second law, i.e. in terms of the total entropy generation rate of the components in the system (equation 3.61 – the objective function).

$$\dot{W}_{net(FirstLaw)} = \dot{m}c_{p,7-8}(T_7 - T_8) - \dot{m}c_{p,1-2}(T_2 - T_1) \quad (5.17)$$

These maximum net power output curves are compared in Figure 5.35. The curves show the results for a system using a concentrator diameter of 8 m with micro-turbine 13 and a

concentrator with 12 m diameter using micro-turbine 32. The first and second law curves compare very well. This means that the second law net power output was accurately modelled in terms of the total entropy generation rate of the system. The small difference can be due to the entropy generation rate in the ducting of the system, which was not accurately modelled.

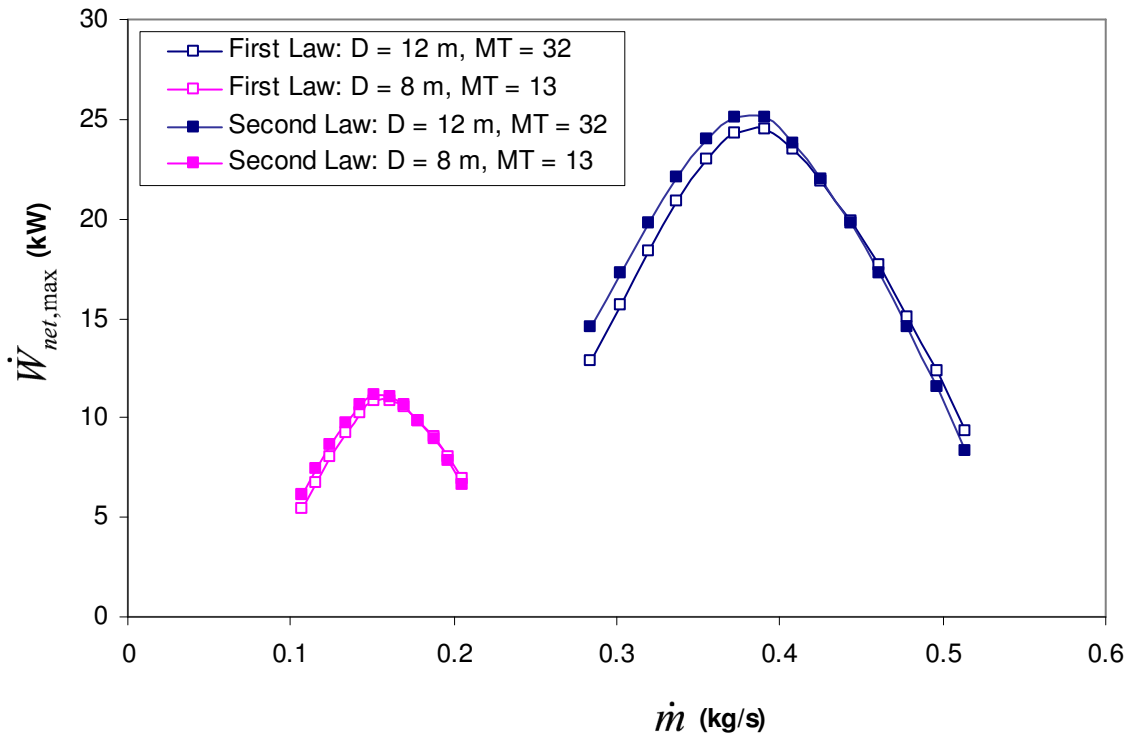


Figure 5.35 Comparison of net power output calculated for two optimised systems using the first and second laws of thermodynamics. The one system uses  $MT = 13$  with  $D = 8$  m and the other uses  $MT = 32$  with  $D = 12$  m.

### 5.3.5 The effect of the changing of a constant on the maximum net power output, optimum geometry and optimum operating conditions of the system

Consider again the constants from Table 5.2. In this section, these constants are considered as the default settings. The results shown in this section are for systems where one of these constants was changed. Table 5.5 shows the values that were changed one at a time for two specific micro-turbine and concentrator diameter combinations to see what effect it would have on the optimum geometry and operating conditions of the system.

Figures 5.36 and 5.37 show the maximum net power output for micro-turbine 13 with  $D = 8$  m and micro-turbine 32 with  $D = 12$  m, where the results using the default settings and changed constants are compared. It is concluded that a temperature decrease and pressure increase of the surroundings increase the maximum net power output. The decrease in maximum net power output due to wind, decreased specular reflectivity, concentrator error, recuperator material

conductivity and increased concentration ratio minimum are shown. A higher concentration ratio decreases the maximum net power output because the size of the receiver decreases as the concentration ratio increases. The results shown in Figures 5.36 and 5.37 are expected to be similar for all the other configurations of concentrator diameter and micro-turbine.

**Table 5.5 Each constant is changed to a new value to see the effect of the changing of one constant.**

	$D = 8 \text{ m}, MT = 13$	$D = 12 \text{ m}, MT = 32$	Unit
$T_0$	308	288	K
$P_1$	100	100	kPa
$I$	1 200	800	$\text{W/m}^2$
$w$	10	10	-
$\varphi_{rim}$	60	30	degrees
$\beta$	30	60	degrees
$e_p$	0.035	0.035	mrاد
$T_{s,max}$	1 100	1 100	K
$refl$	0.98	0.8	-
$k$	237	237	$\text{W/mK}$
$H$	0.5	2	m
$L_{reg,max}$	8	12	m
$CR_{min}$	500	1 000	-

A decrease in rim angle and receiver inclination makes no difference to the maximum net power output. It does, however, make a big change in the optimum receiver geometry variables. For a higher maximum allowable receiver temperature, the maximum net power output is higher. The increase of recuperator length and irradiance results in an increase in maximum net power output. The change in recuperator height makes no difference to the maximum net power output, but it changed the optimum dimensions of the recuperator. Take note how the receiver and recuperator geometry variables are altered due to wind, the doubling of recuperator height and minimum concentration ratio, in Figures 5.38 and 5.39 (for  $D = 12 \text{ m}$  and  $MT = 32$ ). For heavy wind, high concentration ratio, changed inclination and rim angles, it is more beneficial for the system to have a smaller receiver tube diameter (Figure 5.38). In Figure 5.39, it is shown that a doubled recuperator height decreases the optimum recuperator channel aspect ratio tremendously.

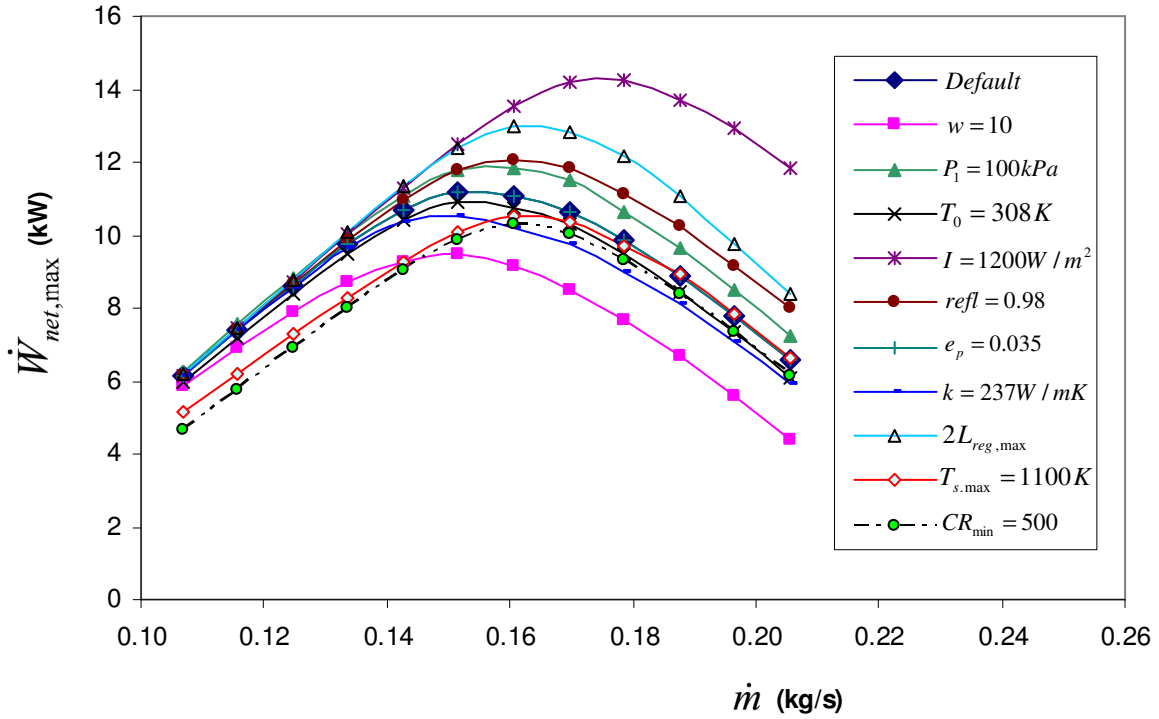


Figure 5.36 Change in maximum net power output for system using  $MT = 13$  and  $D = 8$  m.

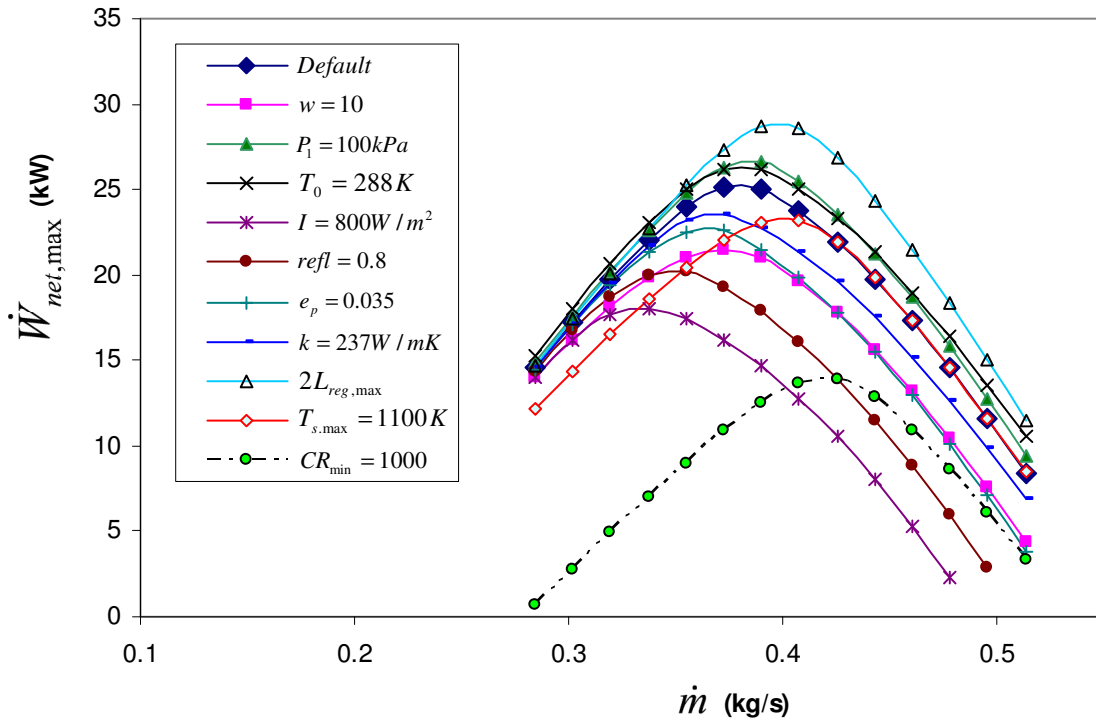


Figure 5.37 Change in maximum net power output for system using  $MT = 32$  and  $D = 12$  m.

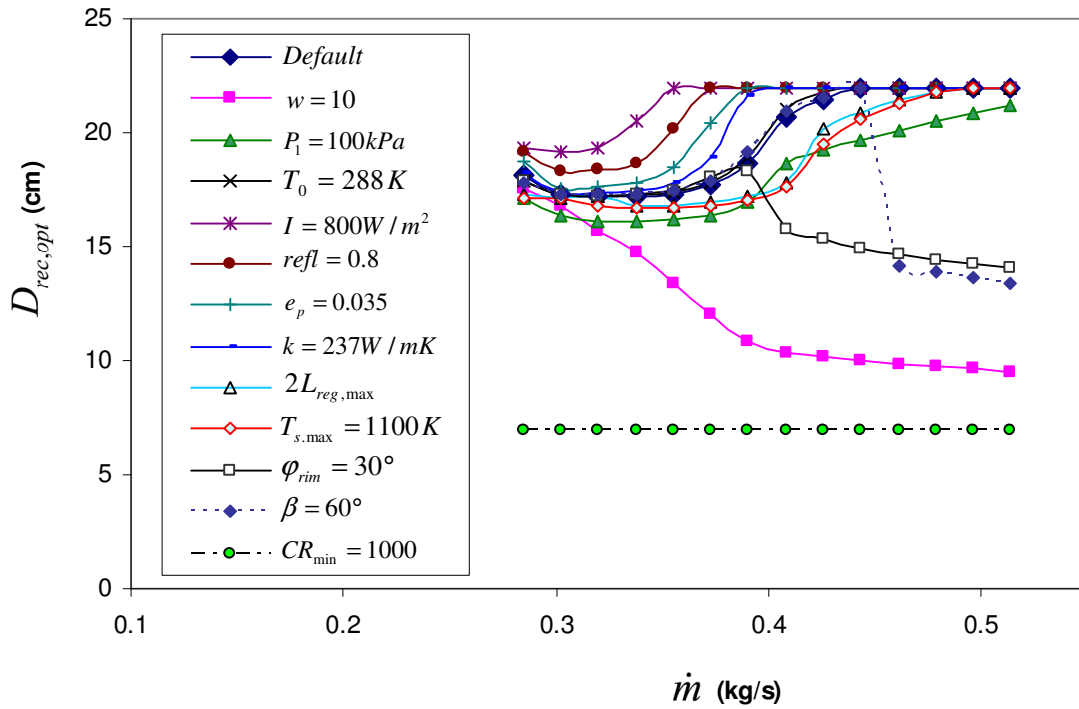


Figure 5.38 Change in optimum receiver tube diameter due to changes in constants for  $D = 12$  m and  $MT = 32$ .

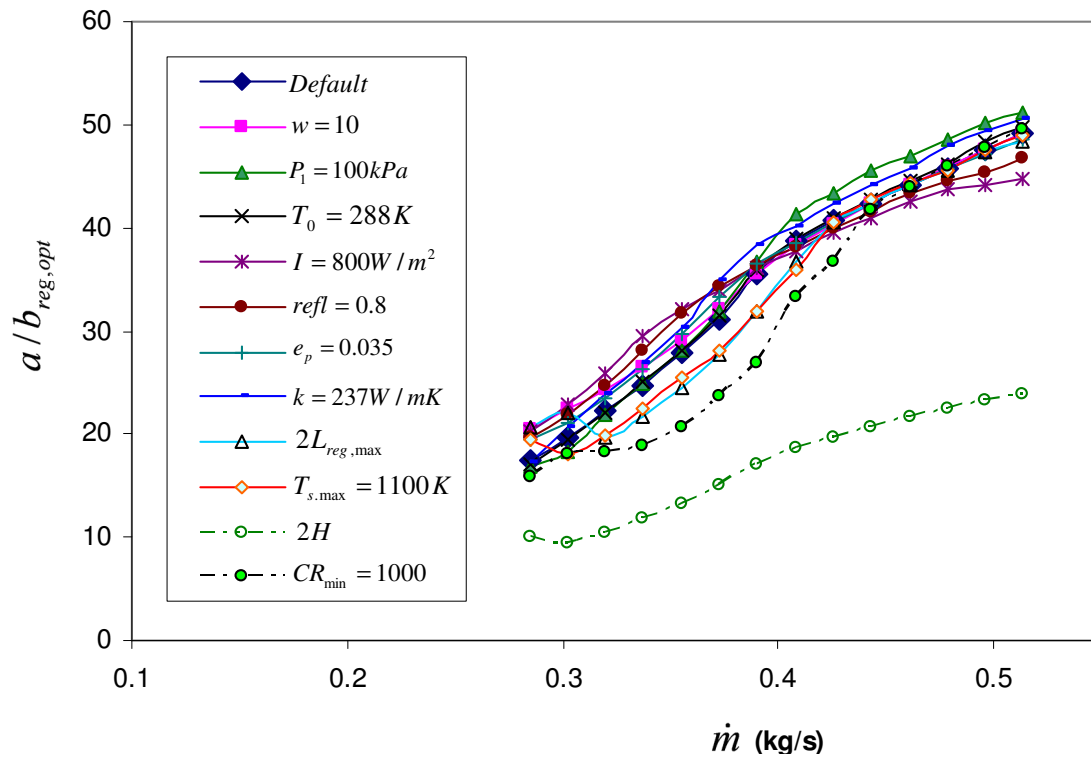


Figure 5.39 Change in optimum recuperator channel aspect ratio due to changes in constants for  $D = 12$  m with  $MT = 32$ .

Consider Figures 5.40 and 5.41. The effect of a few selected constants on the mass flow rate of a recuperator channel is shown for both the configurations. A lowest optimum recuperator mass

flow rate exists. Also note how these figures compare with Figure 5.22. Note how this minimum is shifted due to the constants. It was found that the operating point at this minimum does not necessarily provide the highest maximum net power output. A doubled recuperator length, halved recuperator height, high minimum concentration ratio and higher irradiance shift the maximum recuperator mass flow rate to a higher value and a different system mass flow rate (compare with Section 5.3.3).

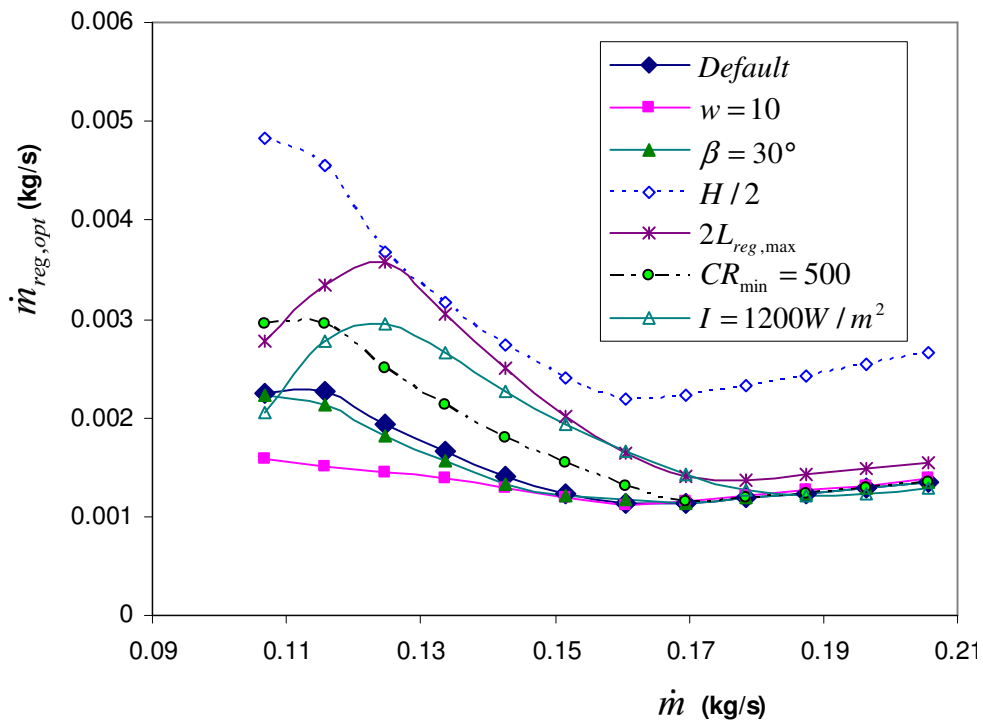


Figure 5.40 Optimum recuperator channel mass flow rate with changes in constants for  $D = 8$  m with  $MT = 13$ .

Now consider Figures 5.42 and 5.43. Here the optimum recuperator  $NTU$  is shown for  $D = 8$  m, using micro-turbine 13 and  $D = 12$  m with micro-turbine 32. In both of these figures, the extended recuperator length increases the maximum of the optimum  $NTU$ . The effect of the wind was to increase the optimum  $NTU$  slightly at lower system mass flow rates. The effect of higher minimum concentration ratio was to decrease the optimum  $NTU$  at smaller mass flow rates. The effect of irradiance at lower mass flow rates was to increase or decrease the optimum  $NTU$  as the irradiance decreased and increased respectively. At higher mass flow rates, the effect was opposite. The other changes did not affect the optimum  $NTU$  much.

Note that the highest maximum net power output for the default settings in Figures 5.36 and 5.37 is at a mass flow rate of 0.15 and 0.375 respectively. When looking at the optimum operating conditions of these mass flow rates, the net power output is not necessarily a maximum when the

$NTU$  is at its highest. This confirms that an optimum condition for an individual component in a system does not necessarily guarantee an optimum net power output, as was emphasised from the literature.

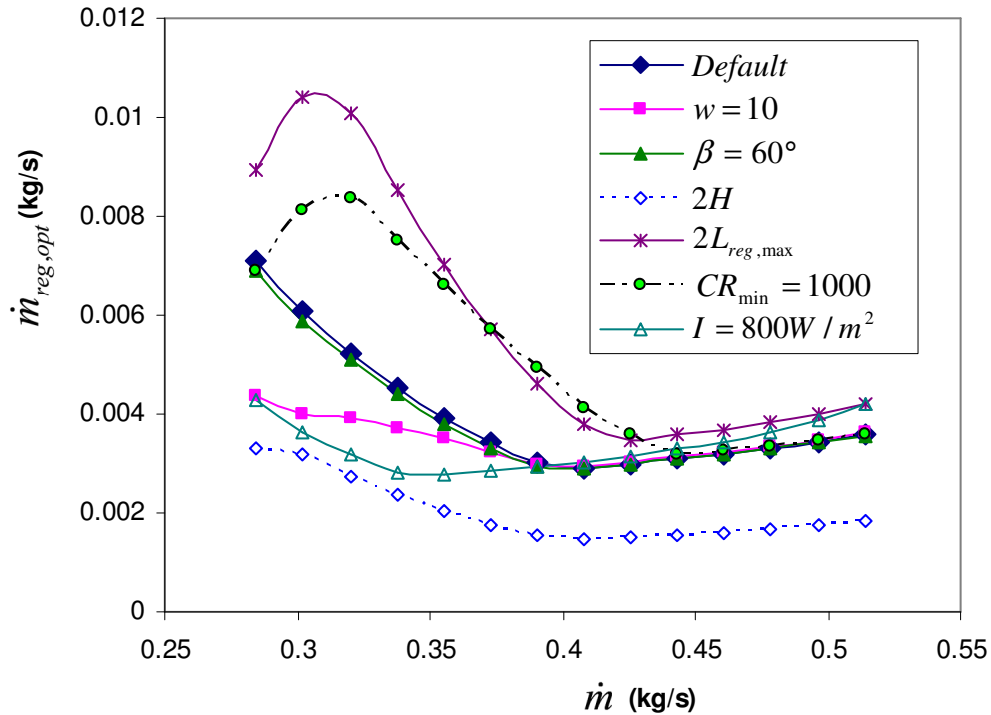


Figure 5.41 Optimum recuperator channel mass flow rate with changes in constants for  $D = 12$  m with  $MT = 32$ .

It is interesting to note that, in some cases, the system property curves do not differ from the default curves and in other cases they differ a lot. A  $60^\circ$  inclination (Figure 5.43) does not do much to the shape of the optimum  $NTU$  but it does, however, change the shape of the optimum receiver tube diameter (Figure 5.38). When considering Figures 5.36 and 5.37 again, the effect due to receiver inclination and recuperator height is not shown. The system variables were altered so that the system can still provide the same maximum net power output for the system with inclined receiver or altered recuperator height. The devastating effect of wind on the system, however, is shown in these figures. The system variables were not able to ‘save’ the maximum net power output, even though the attempts made to do so are shown in all the figures. Note that if the curve for a changed constant is not shown in a figure, it means that it was found to be the same as the default. Some constants do not change the maximum net power output of the system, but the geometry of the recuperator or receiver. This change is due to the optimal spreading of irreversibilities in the different system components. The change of a constant or the change of surroundings can have positive or devastating effects.



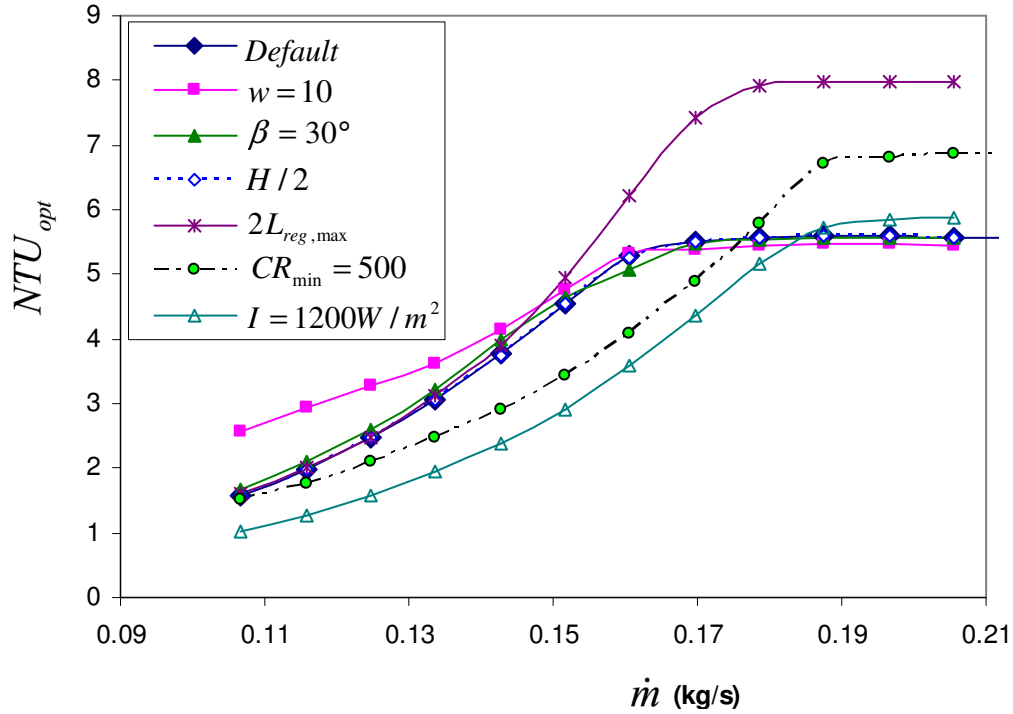


Figure 5.42 The optimum recuperator  $NTU$  with specific scenarios  $D = 8$  m and micro-turbine 13 for changed constants.

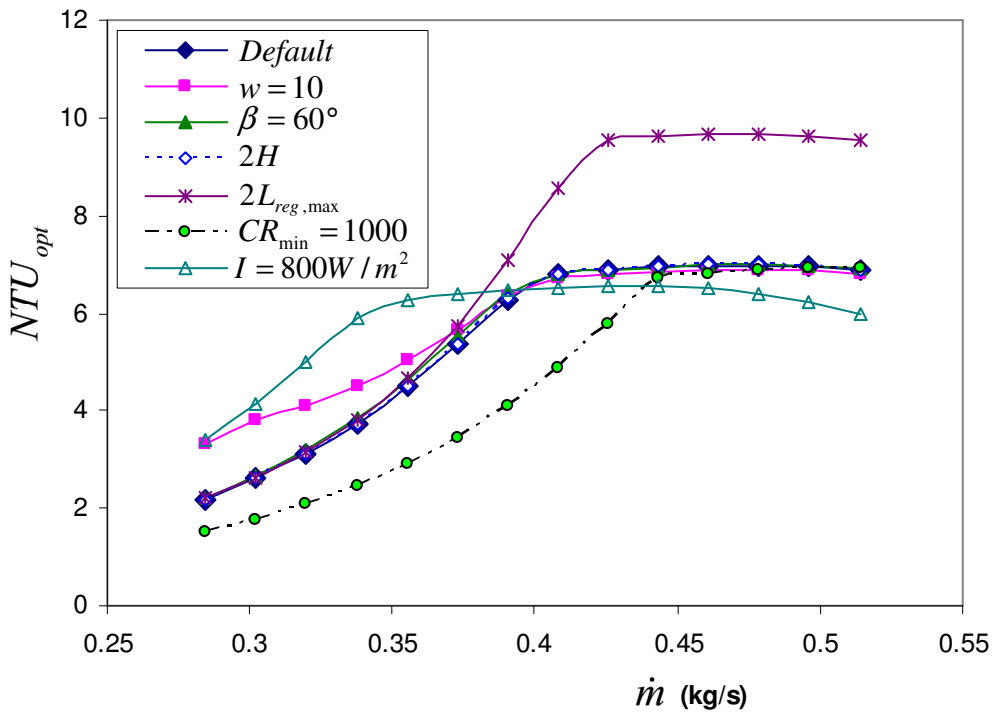


Figure 5.43 The optimum recuperator  $NTU$  with specific scenarios for  $D = 12$  m and micro-turbine 32 for changed constants.

Figure 5.44 shows the effect of environmental conditions and changed constants on the optimum spreading of irreversibilities ( $MT = 41$ ,  $D = 16$  m). Figure 5.45 shows the maximum net power output and minimum irreversibility rates for the default settings. Note that, from above and left in the figures, the following data points are shown: maximum absorbed heat rate, minimum internal and external irreversibility rates and maximum net power output, as shown in Figure 5.26d. Most of the results in Figure 5.44 do not differ much from the results of the default. However, the optimum geometry was usually changed to accommodate for the change in environment or change of situation.

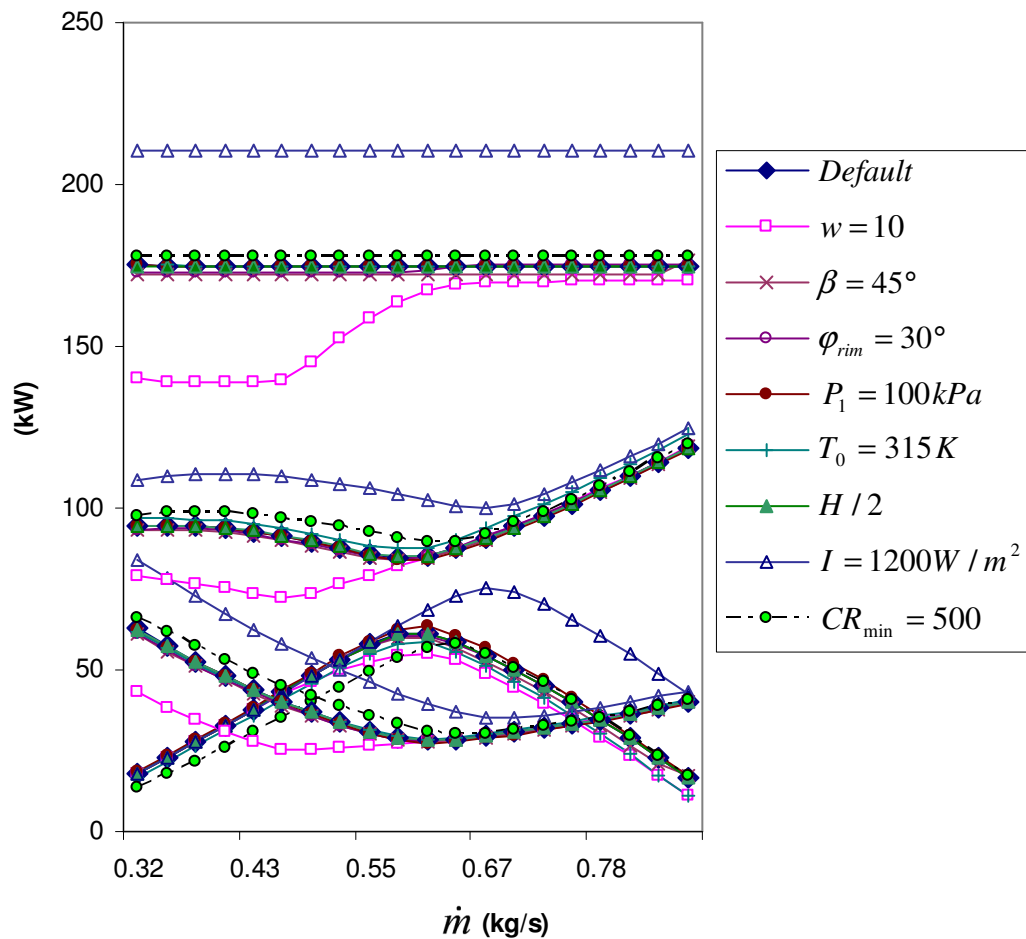


Figure 5.44 The effect of different conditions on the optimum performance of  $MT = 41$  and  $D = 16$  m.

Note that the highest maximum net power output is at the same mass flow rate as where the minimum internal and external irreversibility rates are lowest. This was not the case for extreme wind since the wind affects the absorbed heat rate at smaller system mass flow rates. The wind calls for a smaller aperture diameter, which constrains the rate of heat absorbed. Note that  $C_w$

(see Section 5.3.3) is again approximately three, even for extreme conditions such as an irradiance of  $1\,200\text{ W/m}^2$ , extreme wind and large concentration ratio.

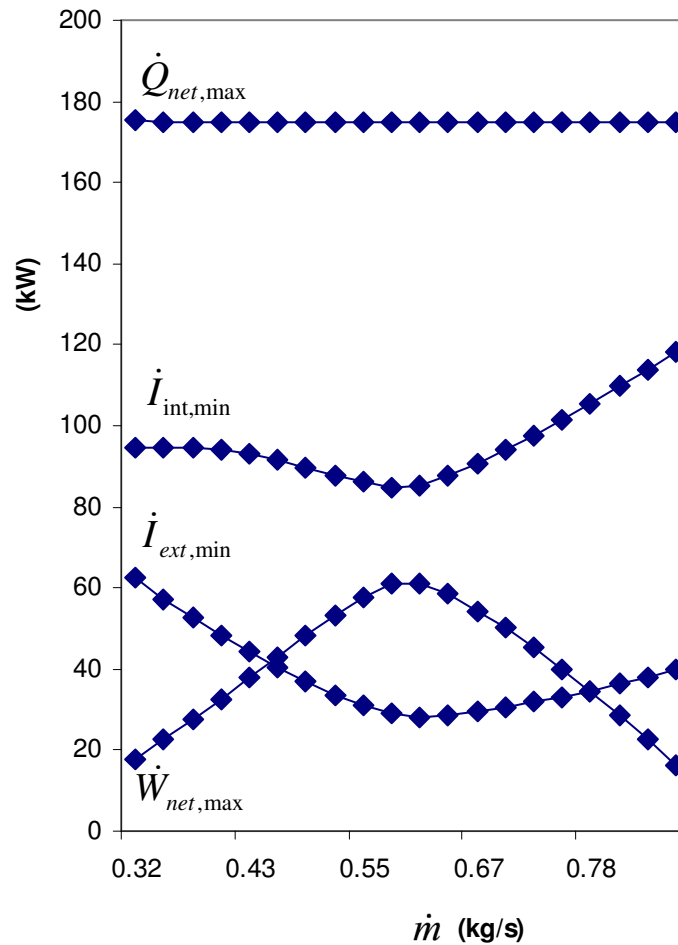


Figure 5.45 Maximum net power output and minimum irreversibility rates for  $D = 16\text{ m}$  with  $MT = 41$ .

In Figure 5.45, the data point where  $\dot{m} = 0.607\text{ kg/s}$  (or  $r = 2.4$ ) gives the maximum net power output of  $61.2\text{ kW}$  with an optimum geometry of  $D_{rec,opt} = 0.2\text{ m}$ ,  $L_{rec,opt} = 61\text{ m}$ ,  $a/b_{reg,opt} = 56$ ,  $D_{h,reg,opt} = 6\text{ mm}$  and  $L_{reg,opt} = 8\text{ m}$ . This optimum geometry was found using the optimisation algorithm and objective function where  $r = 2.4$  is a parameter. A validation is done by changing these variables, one at a time, from the optimum values as shown above. When one of the variables is changed, the other variables stayed constant at their optimum points. Figures 5.46 and 5.47 show the net power output as a function of changing receiver tube diameter and receiver tube length respectively. The total irreversibility rate ( $T_0 \dot{S}_{gen,(int+ext)}$ ) and the net rate of heat absorbed are also shown. In Figure 5.46, the constraints are  $D_{rec} \leq 26.37\text{ cm}$ ,  $D_{rec} \leq 32.5$

cm and  $17 \leq D_{rec} \leq 21$  cm, from Constraint 1, 3 and 4 respectively (see Section 3.8). In Figure 5.47 the constraints are  $L_{rec} \leq 78$  m,  $L_{rec} \geq 39$  m and  $L_{rec} \geq 61$  m, from Constraints 1, 3 and 4 respectively. These graphs show that the maximum net power output is at the point where the total irreversibility rate is a minimum. The maximum net power output in each of these graphs, however, depends on the constraints.

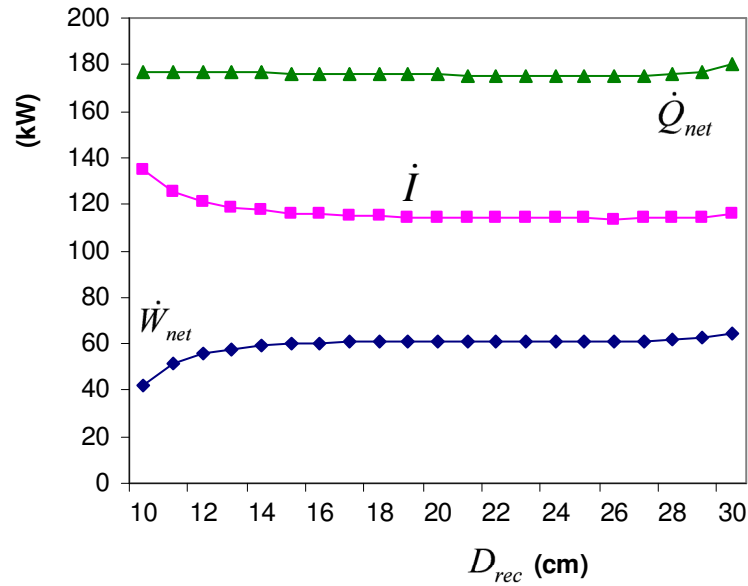


Figure 5.46 Validation of the optimum receiver tube diameter.

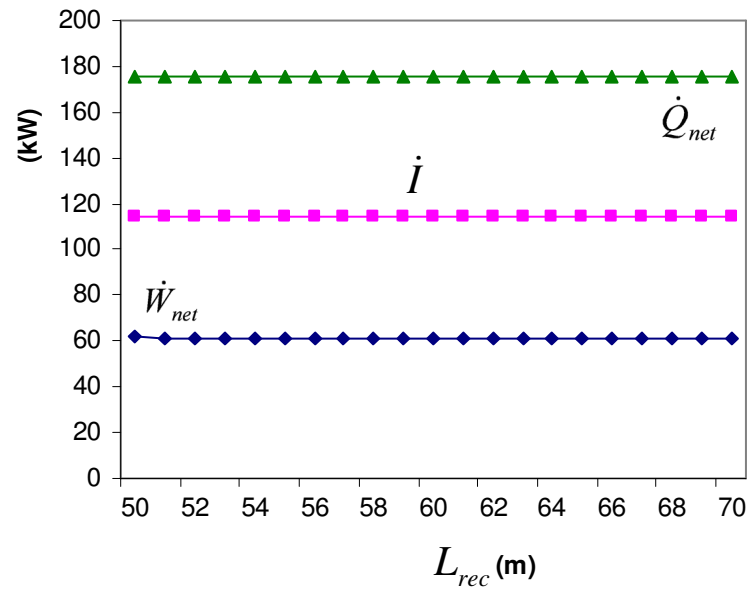


Figure 5.47 Validation of the optimum receiver tube length.

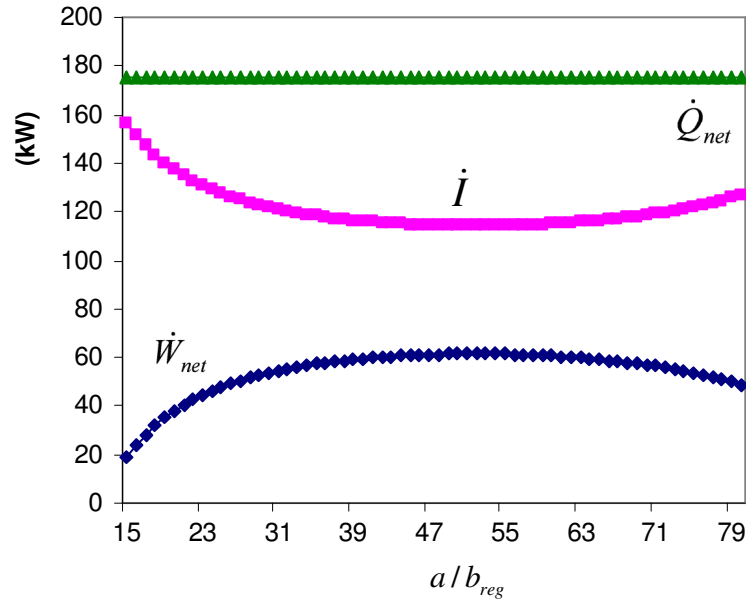


Figure 5.48 Validation of the optimum recuperator channel aspect ratio.

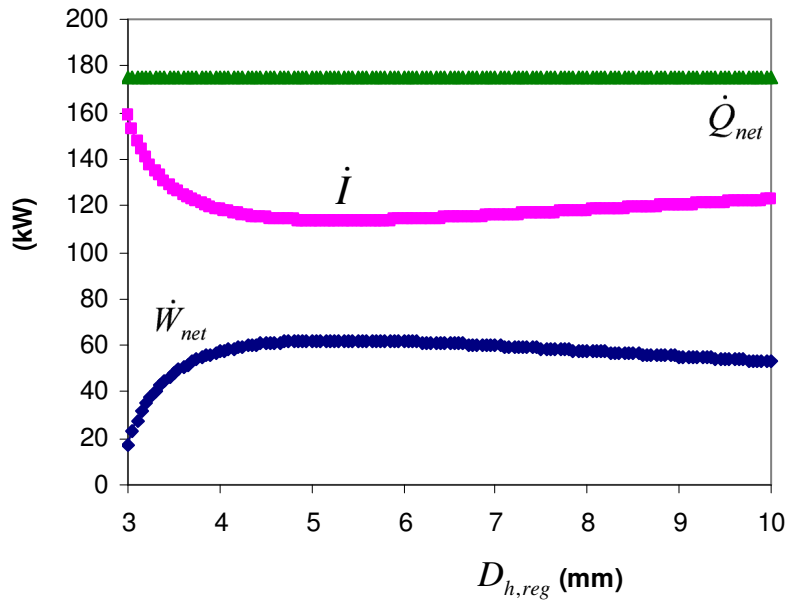


Figure 5.49 Validation of the optimum recuperator channel hydraulic diameter.

Figures 5.48, 5.49 and 5.50 show the net power output, total irreversibility rate and net absorbed power for changing recuperator geometry variables. Once again the net power output and total irreversibility rate mirror each other. In Figure 5.48, the constraint is  $a/b_{reg} \geq 56$  as was set from Constraint 4. In Figure 5.49, the constraint is  $D_{h,reg} \geq 6.2$  mm from Constraint 4. Figure 5.50 has

the constraint of  $L_{reg} \leq 8$  m from Constraints 4 and 7. The optimum geometry for maximum net power output, in each of these graphs, also depends on the constraints.

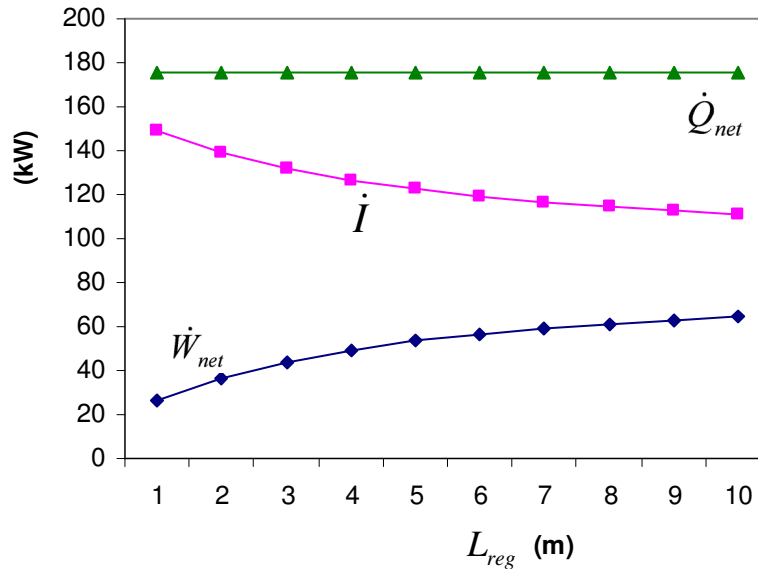


Figure 5.50 Validation of the optimum recuperator length.

These figures confirm that the optimum geometry variables found with the optimisation algorithm are indeed the optimum variables which give maximum net power output of the system. It is also confirmed that the net power output as a function of each of the geometry variables has a maximum at the same position as where the total irreversibility rate is a minimum.

### 5.3.6 Future work

There are many possibilities regarding future work. This work only focused on the open and direct solar thermal Brayton cycle. Similar work can be done on a closed and direct solar thermal Brayton cycle with different working fluids. Similarly, work can be done on indirect cycles. More heat exchangers can be included in the model (multistaging) and their geometries could also be optimised for maximum system net power output using the method of entropy generation minimisation.

Another interesting possibility would be to not only look at a steady-state process, but to include the transient, since the sun's irradiance changes throughout the day. An optimum geometry must exist for the components in the open and direct solar thermal Brayton cycle at a specific location, so that the yearly and daily average net power output of the system is a maximum.

In this work, the compressor and turbine efficiencies were chosen to be at their maximum by selecting a specific range of operating conditions. Since it was found that an individual component in a system should not necessarily operate at its optimum, other operating ranges, which give lower compressor and turbine efficiencies, should also be investigated.

In this study, only standard (off-the-shelf) micro-turbines were used. The geometries of the compressor and turbine can also be included for optimisation to produce maximum net power output of a system at a specific location.

The entropy generation rate in the ducts can be more accurately modelled by adding the duct diameters and lengths as variables in the objective function. One would expect to find that some ducts would be required to be larger or longer than others so that the net power output of the system can be a maximum.

Further constraints can be added to the optimisation algorithm, especially cost constraints. Further size constraints and different receiver and recuperator designs can be incorporated to establish an exceptionally compact solar thermal power system.

This work and the future work that might sprout from it, have the potential of a user-friendly software which asks the user for the properties of the specific location where a solar thermal power system is to be installed. The software would then calculate the optimum geometry of the components required for the system. The groundwork for such software was done in this study (Appendix C) without the user-friendliness.

The results found in this work (the analytical approach) should be compared with experimental work.

# Chapter 6

## Conclusion

---

Southern Africa has a lot of potential to generate large amounts of its power from small-scale and large-scale solar power. The small-scale open and direct solar thermal Brayton cycle with recuperator has several advantages, including lower cost, low operation and maintenance costs and high recommendation. The main disadvantages of this cycle are the pressure losses in the recuperator and receiver, turbomachine efficiencies and recuperator effectiveness, which limit the net power output of such a system. The method of entropy generation minimisation can be used to tackle these disadvantages to optimise the receiver and recuperator and to maximise the net power output of the system.

In this work, a modified cavity receiver and a counterflow plate-type recuperator were optimally sized so that the solar thermal power system can have maximum net power output at steady-state. Two construction methods were considered for this receiver: a circular tube and a rectangular channel. A sizing algorithm was used to establish the net absorbed heat rate of the cavity receiver as a function of the cavity aperture diameter for a specific concentrator diameter with fixed focal length and rim angle. As a result, a specific geometry of the cavity receiver would fix the amount of power absorbed.

Off-the-shelf micro-turbines, operating in their range of maximum compressor efficiency, were considered in the analysis. These micro-turbines and its technical data are freely available in South Africa. The operating point in the range of maximum compressor efficiency, specific micro-turbine and concentrator diameter were used as parameters in the analysis. Forty-five different micro-turbines and seven concentrator diameters between 6 and 18 metres were considered. For each set of parameters an objective function, the net power output, was maximised by optimising geometry variables of the modified cavity receiver and counterflow plate-type recuperator. This optimisation was done with limiting constraints. The dynamic trajectory optimisation method for constrained optimisation was used.

An exergy analysis of the solar thermal power system, identification of total entropy generation within the system and an iteration to determine the temperatures and pressures at each point in the system in terms of geometry variables, were used to establish the objective function. The net power output of the system was described in terms of the total entropy generation within the



system. The constraints on the objective function included constraints on maximum recuperator length and minimum concentration ratio between receiver aperture area and concentrator area. A maximum receiver surface temperature of 1 200 K was set. An average irradiance of 1 000 W/m<sup>2</sup> was assumed. Systems with a 45° concentrator rim angle and a receiver aperture in the horizontal plane, were analysed.

The optimum recuperator channel aspect ratio for the counterflow plate-type recuperator with a constant recuperator height was found to be a linear function of the system mass flow rate. Other studies have found that, for a rectangular channel, an aspect ratio of eight should be used for minimum entropy generation in the channel. In this work, however, results showed that an aspect ratio of eight is not necessarily the optimum aspect ratio for the receiver and recuperator channels in a system which should produce maximum net power output. This is the result of minimising total entropy generation for the whole system, instead of for components individually.

Results showed that the optimum recuperator length increased as a function of mass flow rate until the length constraint was reached. The same result was found for optimum *NTU*. It was concluded that for maximum system net power output at lower system mass flow rates, it is more beneficial to have a low recuperator efficiency (or a bypassed recuperator). This result validated that a high efficiency for an individual component in a system does not necessarily provide optimum results for the system as a whole. When maximum net power output is required, it is in some cases better for the system to have a component with low efficiency.

No major differences could be found in the maximum net power output between cavity receivers constructed with a rectangular channel and cavity receivers constructed with a circular tube respectively. It was found that a large solar cavity receiver aperture or a small rectangular channel aspect ratio, but not necessarily both, is most beneficial. It was also found that the receiver tube diameter should be relatively large. For the circular tube and rectangular channel receiver, the optimum number of tube diameters or rectangular channels that should fit in between the aperture edge and the receiver edge was found.

Optimum system operating conditions were established in the analysis. The results showed how the irreversibilities should be spread throughout the system optimally in order for the system to produce maximum net power output. The optimum recuperator channel mass flow rate, receiver hydraulic diameter and optimum *NTU* behaved very specifically with the system mass flow rate. It was found that it is best for the receiver to operate in the turbulent flow regime, and for the recuperator channels to operate in the laminar flow regime. Results showed that at higher mass flow rates, the maximum receiver surface temperature decreased as a function of mass flow rate.

It was noted that the minimum rate of internal irreversibility of the optimised systems was always more than the minimum rate of external irreversibility. It was found that the solar receiver is the main contributor to the total rate of internal entropy generation for the optimised systems with maximum net power output. Results showed that the irreversibilities were spread throughout the system in such a way that the minimum internal irreversibility rate was almost three times the minimum external irreversibility rate for all data points, which gave the highest maximum net power output of a micro-turbine. A constant was given for this optimum ratio of minimum internal irreversibility rate to minimum external irreversibility rate ( $C_w$ ), where the maximum net power output in a micro-turbine's operating range is the largest (at optimum operating point of a micro-turbine). Results showed that  $C_w$  increases as the mass flow rate increases for a specific concentrator diameter. The highest maximum thermal efficiency of these optimised systems was found to be a function of the solar concentrator diameter and choice of micro-turbine.

The effect of various conditions such as wind, receiver inclination, concentrator rim angle and irradiance on the maximum net power output and optimum geometries of the system components was investigated. The maximum net power output was found to stay constant in certain cases while the optimum geometry was shifted around to accommodate for the change. This was observed in changes in recuperator height, receiver inclination and concentrator rim angle. In other cases, the maximum net power output could be changed by changing a constant such as the effect of wind, irradiance, minimum concentration ratio, recuperator length, surrounding pressure, recuperator material and maximum surface temperature. Results showed that, for a specific environment and parameters, an optimum receiver and recuperator geometry exists so that the system can produce maximum net power output.

It was found that the second law of thermodynamics is a valuable contribution to the optimisation of solar thermal power systems. The geometry of components in a solar thermal power system should be optimised by minimising the total rate of entropy generation in the system in such a way that the system produces maximum net power output. The results of this study give insight into the optimal behaviour and component geometries of the recuperative solar thermal Brayton cycle limited to challenging constraints. These results can be considered in the preliminary stages of design. The results found in this work (the analytical approach) should be compared with experimental work. The small-scale open and direct solar thermal Brayton cycle with optimised geometry for maximum net power output, using the method of entropy generation minimisation, can be regarded as a good local power generation method for the near future.